The Astrophysical Journal, 733:23 (19pp), 2011 May 20 doi:10.1088/0004-637X/733/1/23

TWELVE AND A HALF YEARS OF OBSERVATIONS OF CENTAURUS A WITH THE *ROSSI X-RAY TIMING EXPLORER*

R. E. Rothschild[1], A. Markowitz[1], E. Rivers[1], S. Suchy[1], K. Pottschmidt[2,3], M. Kadler[4], C. Müller[4], and J. Wilms[4]
[1] Center for Astrophysics and Space Sciences, University of California, San Diego, CA 92093-0424, USA;
rrothschild@ucsd.edu, almarkowitz@ucsd.edu, erivers@ucsd.edu, ssuchy@ucsd.edu
[2] CSST, University of Maryland Baltimore County, 1000 Hilltop Circle, Baltimore, MD 21250, USA; katja@milkyway.gsfc.nasa.gov
[3] CRESST and NASA Goddard Space Flight Center, Astrophysics Science Division, Code 661, Greenbelt, MD 20771, USA
[4] Dr. Remeis Sternwarte & ECAP, Sternwartstr. 7, 96049 Bamberg, Germany; matthias.kadler@sternwarte.uni-erlangen.de,
cornelia.mueller@sternwarte.uni-erlangen.de, joern.wilms@sternwarte.uni-erlangen.de
Received 2010 November 5; accepted 2011 March 11; published 2011 April 29

ABSTRACT

The *Rossi X-ray Timing Explorer* (*RXTE*) has observed the nearest radio galaxy, Centaurus A (Cen A), in 13 intervals from 1996 August to 2009 February over the 3–200 keV band. Spectra accumulated over the 13 intervals were well described with an absorbed power law and an iron line. Cutoff power laws and Compton reflection from cold matter did not provide a better description. For the 2009 January observation, we set a lower limit on the cutoff energy at over 2 MeV. The power spectral density function was generated from *RXTE*/All Sky Monitor and Proportional Counter Array data as well as an *XMM-Newton* long look, and clear evidence for a break at 18^{+18}_{-7} days (68% conf.) was seen. Given Cen A's high black hole mass and very low value of L_X/L_{Edd}, the break was a factor of 17^{+36}_{-13} times higher than the break frequency predicted by the McHardy et al. relation, which was empirically derived for a sample of objects, which are radio-quiet and accreting at relatively high values of L_{bol}/L_{Edd}. We have interpreted our observations in the context of a clumpy molecular torus. The variability characteristics and the broadband spectral energy distribution, when compared to Seyferts, imply that the bright hard X-ray continuum emission may originate at the base of the jet, yet from behind the absorbing line-of-sight material, in contrast to what is commonly observed from blazars.

Key words: galaxies: active – galaxies: individual (Centaurus A, NGC 5128) – galaxies: jets – X-rays: galaxies

Online-only material: color figures

1. INTRODUCTION

The prototype Fanaroff–Riley Class I (FR I; Fanaroff & Riley 1974) low-luminosity radio source Centaurus A (hereafter Cen A) played a significant role in the early understanding of the nature of active galaxies and jet emission. Cen A was found to "correspond within limits of experimental error" to the "extra-galactic nebula" NGC 5128 by Bolton et al. (1949). Early radio interferometry by Mills (1952) established that Cen A was an extended source and therefore not a stellar object. In addition, Mills found it to be nearly 2° in diameter in radio with "a strong concentration near its center." A year later, Mills (1953) refined the sizes to 1°.5 for the extended flux and 5′ for the compact core. Arguments by Baade & Minkowski (1954) demonstrated that Cen A was extragalactic, and Humason et al. (1956) revealed an uncorrected redshift close to the present-day value ($z = 0.001825$). The giant radio lobes were resolved by Wade (1959) after removal of the bright compact source coincident with NGC 5128. The synchrotron nature of the radio emission was put forth by Shklovsky and collaborators (see, e.g., Burbidge & Burbidge 1957, for references).

The Centaurus region of the southern sky was scanned in the late 1960s by rocket and balloon X-ray payloads without detecting Cen A (Cooke et al. 1967; Harries et al. 1967; Lewin et al. 1968). The 1969 rocket flight of Bowyer et al. (1970) was the first claimed detection, and was followed by many rocket, balloon, and satellite observations (see Stark et al. 1976, for a list of early results). A power-law continuum with a photon index of $\Gamma \sim 1.8$ extending beyond 200 keV was soon established with low-energy absorption due to intervening matter having an equivalent hydrogen column density, N_H, along the line of sight near 10^{23} atoms cm^{-2} (e.g., Baity et al. 1981). *Compton Gamma Ray Observatory* (*CGRO*) observations of Cen A extended the flux detections to 1 MeV (Kinzer et al. 1995) and to greater than 100 MeV (Steinle et al. 1998). Recently, emission from the core of Cen A (Abdo et al. 2010b) and its extended emission (Abdo et al. 2010a) have been detected by the *Fermi*/Large Area Telescope at GeV energies, and by H.E.S.S. at TeV energies (Aharonian et al. 2009), further extending the detected emissions from this remarkable object over the entire electromagnetic spectrum.

By virtue of being the nearest radio galaxy and one of the few bright active galaxies in the 2–10 keV X-ray band, detailed X-ray observations of Cen A revealed much about the nuclei of low-power, radio-loud active galaxies in general (see Israel 1998, for a review). With present-day imaging instruments, we have a remarkably detailed view of Cen A. *Chandra*'s spectacular images have revealed details for a wealth of features: jet structure, knots in the jets, discrete sources, and shocks in the interstellar medium (e.g., Kraft et al. 2000, 2001, 2003). Evans et al. (2004) used *Chandra* and *XMM-Newton* observations to conclude that the iron line at 6.4 keV originated in cool material that either surrounds the black hole or forms part of a torus, most of which is out of the line of sight. In either case, the iron emitting region was distant from the central source.

While comparison of the blazar Cen A to Seyfert galaxies is not strictly proper due to jet-dominated blazar spectra versus disk-dominated Seyfert spectra, Cen A displays at least one aspect of disk-dominated spectra, i.e., iron line emission from cold material. The jet-like emission comes from a jet whose

primary beam is oriented far from the observer's line of sight and thus some Seyfert-like aspects of the spectra become detectable. One must keep this in mind when comparing Cen A results to those of Seyfert active galactic nuclei (AGNs) and to those of blazars.

Infrared observations from the ground with adaptive optics and from *Hubble Space Telescope* yielded estimates of the mass of the supermassive black hole from gas kinematics and stellar dynamics (e.g., Silge et al. 2005; Marconi et al. 2006). Integral-field observations in the near-infrared with the SINFONI spectrograph with adaptive optics on the Very Large Telescope gave $M_{\rm BH} = (5.5 \pm 3.0) \times 10^7\,M_\odot$ based upon stellar kinematics and $(4.5^{+1.7}_{-1.0}) \times 10^7\,M_\odot$ from H_2 kinematics (Cappellari et al. 2009; Neumayer et al. 2010). Krajnović et al. (2007), using the CIRPASS spectrograph on Gemini South, found $M_{\rm BH} = (8.25^{+2.25}_{-4.25}) \times 10^7\,M_\odot$ based on gas dynamics. For a distance of 3.42 Mpc (Ferrarese et al. 2007), 3.5 Mpc (Hui et al. 1993), or 3.8 Mpc (Rejkuba 2004; Harris et al. 2010), this mass must be contained within $\simeq$0.6 pc (Marconi et al. 2006). We adopt the values of 3.8 Mpc and $6 \times 10^7\,M_\odot$ for the following analyses and discussions.

Radio observations of the inner tens of parsecs reveal an unresolved core with a jet and counter jet (Horiuchi et al. 2006) with the inner $\pm$20 mas being resolved into multiple components. TANAMI radio observations (Ojha et al. 2010) find that the core region has an inverted spectrum indicative of on-going synchrotron and possible synchrotron self-Compton (SSC) or free–free absorption processes (Müller et al. 2010). While not unexpected, this would support a model of SSC for producing the hard X-ray flux observed (Chiaberge et al. 2001).

With its broadband X-ray coverage, highly maneuverable spacecraft, and flexible scheduling, the *Rossi X-ray Timing Explorer* (*RXTE*) is the premier mission for monitoring and multiple observations of X-ray sources on timescales from milliseconds to years. Multi-timescale monitoring campaigns to probe X-ray variability in AGNs on timescales from hours to years began with the *EXOSAT* era in the 1980s (e.g., Lawrence et al. 1987; Lawrence & Papadakis 1993; Green et al. 1993), and has continued to present day with *RXTE* (e.g., Edelson & Nandra 1999; Markowitz et al. 2003; McHardy et al. 2006). The resulting broadband power spectral density functions (PSDs), derived mainly for radio-quiet "normal" broad line Seyfert 1s and narrow line Seyfert 1s, have yielded evidence for breaks at temporal frequencies $f_{\rm b}$ in the range $\sim 10^{-6}$ to 10^{-3} Hz with PSD power-law slopes breaking from about –2 to about –1 above and below $f_{\rm b}$, respectively. McHardy et al. (2006) and references therein have shown that the temporal variability resulting from accretion onto black holes, as characterized by $f_{\rm b}$, scales inversely with black hole mass and directly with bolometric luminosity. Comparatively less is known about the X-ray variability properties of non-Seyferts, including jet-dominated blazars and radio galaxies such as Cen A. Preliminary X-ray structure functions and PSDs for blazars, though frequently based on long-term light curves which are gap-dominated, have revealed breaks which, like Seyferts, correspond to timescales of a few days to a couple of weeks (Kataoka et al. 2001, 2002; Marscher et al. 2004).

In this paper, we present spectral and timing results on Cen A derived from 13 observations spanning 1996 to 2009 made with *RXTE*. Our goals include characterizing broadband X-ray spectral variability, constraining the geometry of the circumnuclear accreting material by studying both the line-of-sight absorbing gas and the Fe Kα line-emitting gas, and quantifying X-ray variability across a range of timescales in order to better understand Cen A for comparison with other AGNs. The remainder of this paper is structured as follows: Section 2 gives the details of the observations, Section 3 describes data selection and analysis techniques, Section 4 gives the results of spectral and temporal analyses, including a first-ever broadband PSD (covering below $\sim 10^{-5}$ Hz) for Cen A, while Section 5 discusses the results of these observations of Cen A, and finishes with our conclusions.

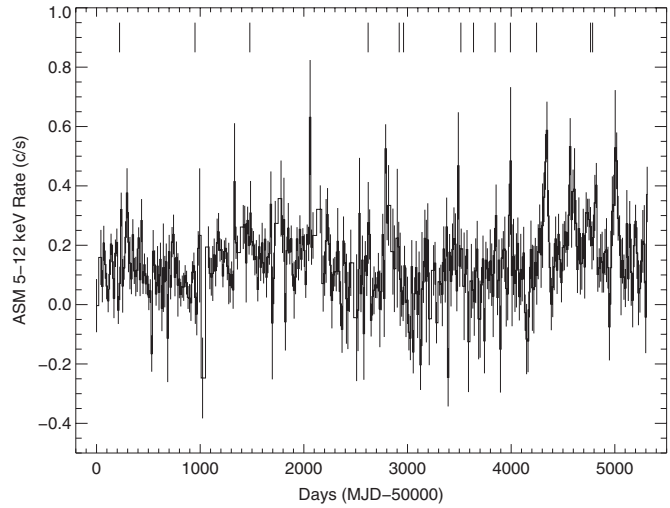

Figure 1. Flux history of Cen A over the *RXTE* mission as measured by the ASM 5–12.1 keV channel 3, with two week binnings. The vertical bars at the top of the plot denote when the *RXTE* pointed observations were made.

2. OBSERVATIONS

The flux history of Cen A over the duration of the *RXTE* mission from 1996 through mid-2010, as measured in the 5–12.1 keV band by the *RXTE*/All-Sky Monitor (ASM; Figure 1), reveals variations of a factor of three or more. Thirteen observing campaigns totaling 129 separate pointings were executed using *RXTE*'s pointed-mode instruments, the Proportional Counter Array (PCA) and the High Energy X-ray Timing Experiment (HEXTE), as indicated in Figure 1. Each campaign consisted of 1 to 22 individual pointings, and spanned durations of less than a day to several days. The 13 campaigns could be divided into observations on 51 separate days (from which 47 daily spectra were produced; see Section 4.2.2), and adjacent campaigns were separated by less than a month to years. We thus have the ability to probe spectral and temporal variability in Cen A on a wide range of timescales, including hours, individual days, and weeks to years.

Table 1 gives the livetimes for the 13 separate observing intervals of Cen A from 1996 August to 2009 February. The counting rates are for 3–60 keV from the top layer of the PCA detector PCU2 and 15–200 keV for HEXTE. Since the on-source/off-source rocking of HEXTE cluster A was terminated on 2006 July 13, the livetimes and rates are given for the combined clusters up to that date as well as just cluster B throughout the mission. See the next section for a description of the PCA and HEXTE.

3. DATA ANALYSIS

Version v6.7 of the HEASOFT software package release[5] with updated PCA response v11.7 (2009 May 11) and

[5] http://heasarc.gsfc.nasa.gov/ftools/

Table 1
Livetimes and Rates for Observations of Cen A with *RXTE*

Date	PCU2 Livetime[a]	PCU2 Rate[b,c]	HEXTE-AB Livetime[a]	HEXTE-AB Rate[b,c]	HEXTE-B Livetime[a]	HEXTE-B Rate[b,c]	Num. Obs.	Num. Days
1996 Aug	10,528	23.24 ± 0.07	6,785	5.12 ± 0.20	3,390	4.88 ± 0.27	1	1
1998 Aug	67,872	21.23 ± 0.03	42,567	4.41 ± 0.08	18,521	3.77 ± 0.12	7	4
2000 Jan	25,088	34.58 ± 0.05	16,132	7.72 ± 0.12	8,037	7.01 ± 0.15	3	1
2003 Mar	75,280	42.46 ± 0.03	58,574	11.52 ± 0.04	29,302	10.40 ± 0.06	13	4
2004 Jan	88,960	24.46 ± 0.04	59,788	6.86 ± 0.04	26,015	6.13 ± 0.05	22	3
2004 Feb	36,112	28.14 ± 0.04	23,680	7.94 ± 0.06	14,405	7.11 ± 0.08	4	2
2005 Aug	9,472	24.95 ± 0.07	6,073	6.47 ± 0.13	3,021	5.53 ± 0.17	1	1
2005 Dec	20,994	19.15 ± 0.07	...	...	7,115	4.50 ± 0.12	8	3
2006 Jul	29,968	33.46 ± 0.04	...	...	9,228	7.04 ± 0.10	22	7
2006 Dec	53,088	25.01 ± 0.03	...	...	16,984	5.04 ± 0.08	15	7
2007 Aug	38,784	46.50 ± 0.04	...	...	12,997	10.44 ± 0.10	11	4
2009 Jan	81,230	64.31 ± 0.03	...	...	27,406	14.91 ± 0.07	15	5
2009 Feb	38,800	63.90 ± 0.05	...	...	12,171	15.03 ± 0.10	7	3

Notes.
[a] The livetime is in seconds.
[b] The PCU2 3–60 keV counting rate is in counts s^{-1}; the HEXTE 15–200 keV counting rate is in counts s^{-1}.
[c] Uncertainties in rates are 68% confidence.

background estimation files Faint/L7 and Sky_VLE dated 2005 November 28 were used throughout, as was XSPEC 12.5.1n (Arnaud 1996). All errors presented are 90% confidence intervals, with the exceptions of iron line equivalent widths, which have 99% uncertainties, and the counting rates in Table 1 are 68% errors.

3.1. Proportional Counter Array

For the PCA (Jahoda et al. 2006), only data from the top layer of the second Proportional Counter Unit (PCU)—PCU2—were used in the present analysis, since its calibration was the most refined of the five PCU counters (Jahoda et al. 2006) and since it was the one PCU in common for all of the Cen A observations. The PCU2 data were accumulated under the conditions that the source was greater than 10° above Earth's limb, the pointing direction was within 0°.01 of the source position, the satellite was more than 30 minutes from the last onset of a South Atlantic Anomaly (SAA) passage, and the veto rate indicative of precipitating electrons was less than 0.1.[6] The PCU2 Standard Data counts histograms were rebinned into wider energy bins above channel 60 by 2, above channel 80 by 4, and above channel 100 by 29 in all analyses. PCU2 data from the full 3–60 keV energy range were subject to fitting for this paper, and no systematic errors were added to the PCU2 data.

The Faint background model was used for all but the 2009 January/February observations, for which the SkyVLE background model was used. The choice of background models was determined by whether or not the PCU2 top layer rate exceeded 50 counts s^{-1}, and only the 2009 January and February rates exceeded this value. The PCU2 background models were calculated from particle rates from the detector based upon numerous blank sky pointings throughout the *RXTE* mission (Jahoda et al. 2006), and as such, individual observations were susceptible to minor differences in normalization between the model background and reality. Similarly, the dead time correction was based upon detector rates and modeled appropriately. In order to adjust spectral analyses for small deviations of the background and dead time models from reality, the background model counts histogram was included in the XSPEC fitting as a correction file (see Section 3.3 for a description of this procedure).

3.2. High Energy X-ray Timing Experiment

The HEXTE (Rothschild et al. 1998) data from on-source and two off-source positions were collected from each cluster separately until the cluster A rocking was discontinued on 2006 July 13. After that the cluster B data were still collected from both off-source positions, but no off-source data were collected from cluster A. The same elevation, pointing accuracy, and time since the SAA criteria were used in the selection of good data for HEXTE. The HEASARC tool HEXTErock was used to determine if a known source would be in any of the HEXTE off-source positions. None were. Consequently, the two background spectral accumulations, when available for cluster A and always for cluster B, were combined to form a single background spectrum for each cluster. The on-source accumulations for both clusters were then combined as well as the appropriate background files. Combining these data sets directly was possible due to the HEXTE automatic and continuous gain control system that allowed for the setting of all detector gains to be the same. This resulted in a single on-source and single background file for each Cen A observation for which both clusters were rocking. In those instances where cluster A was not rocking, only cluster B data were used. No systematic errors were added to the HEXTE data.

HEXTE background files were accumulated in real time during an observation as a result of the HEXTE cluster rocking program, and were not a product of a modeling program. The dead time calculated for each data segment was, however, subject to a model based upon particle event rates, and as such could produce imperfect background subtraction. The same technique for dealing with this effect as for PCU2 was used, and the correction amounted to less than 1% in all cases (Figure 2). The HEXTE data were rebinned by 5 above channel 60, by 10 above channel 160, and by 20 above channel 210. HEXTE data from 18–200 keV were used in this paper.

3.3. Simultaneous PCA and HEXTE Spectral Fitting

Simultaneous fitting of the PCU2 and HEXTE data was performed on both daily and the 13 observation interval data

[6] http://heasarc.gsfc.nasa.gov/docs/xte/recipes/pca_event_spectra.html#reduction

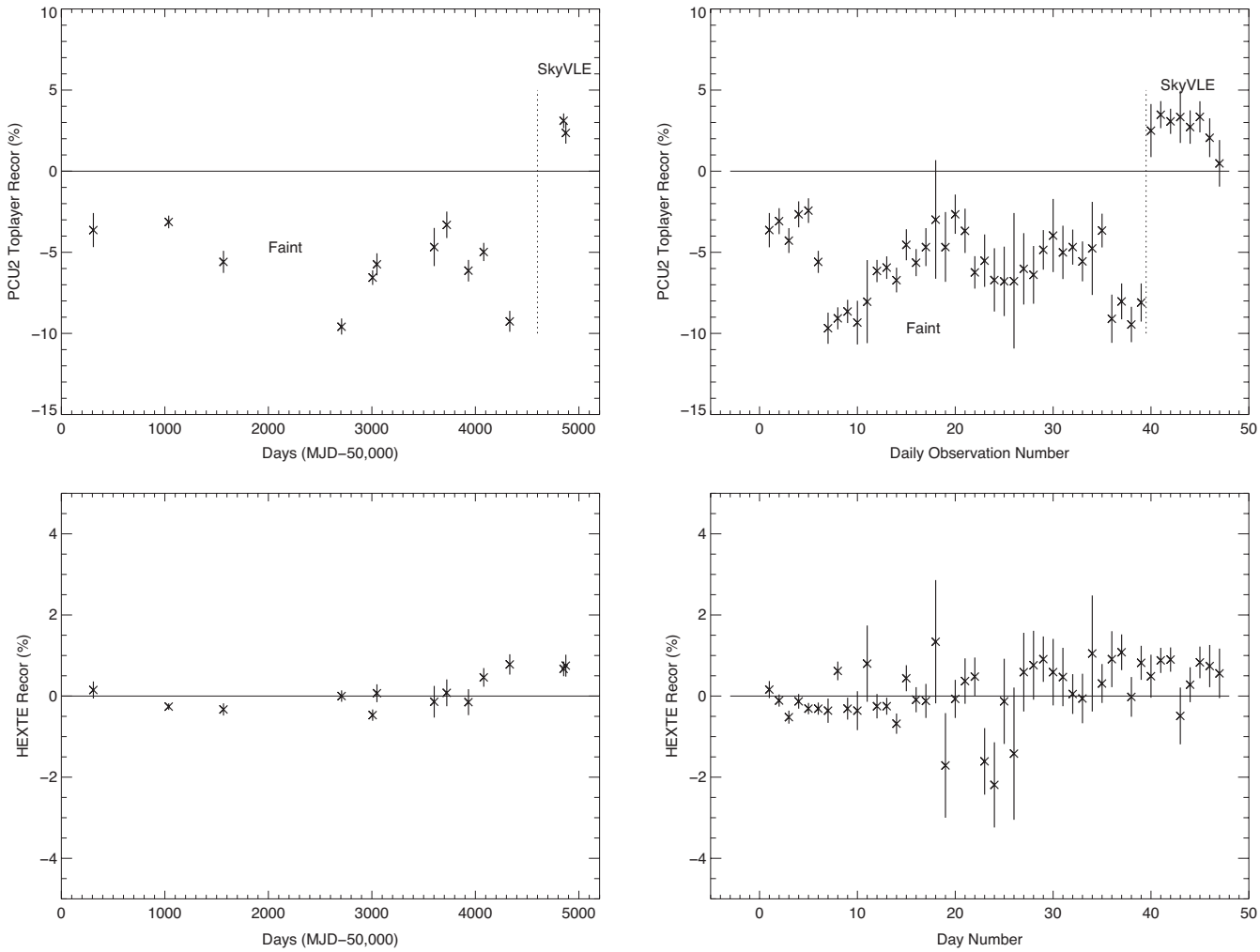

Figure 2. Best-fit correction factors applied to background/dead time estimates for the 13 observation intervals and the 47 daily spectra histograms for PCU2 (top) and HEXTE (bottom) derived from fitting of Cen A spectra. The vertical dotted line in the PCU2 figures delineates the separation of Faint and SkyVLE background estimate use. Horizontal lines at a value of zero are included.

where the HEXTE data had sufficient statistical quality to affect the result. This provided the best-fit *RXTE* broadband 3–200 keV spectral parameters for Cen A with overlapping PCU2 and HEXTE data in the 18–60 keV band. A constant multiplying the HEXTE model was fitted to correct for the relative normalization of HEXTE with respect to PCU2. The fitted value of this constant was about 80% for the observations. This reflected the differences in assumed Crab normalization between PCA and HEXTE, where the PCA normalization is assumed in the reported fluxes.

When fitting Cen A data using `XSPEC 12.5.1n` (which allows for use of background correction files for more than one detector), the correction factor for imperfect knowledge of the PCU2 background and PCU2 and HEXTE dead time estimates was an integral part of the fitting procedure, and in this manner uncertainties in the correction were included in the calculation of parameter uncertainties. The use of this procedure required that the `XSPEC` parameter `delta`, which defines the step size used in numerical determination of the derivatives used in the fitting process, be set to 1×10^{-4} (K. Arnaud 2010, private communication) and that numerical differentiation be used (its value in the `.xspec/Xspec.init` file must be set to true[7]). The resulting negative values of the PCU2 corrections for the first 11 observation intervals ranged from a few to less than 10%, which is consistent with the values found by Rothschild et al. (2006) for the first six *RXTE*/PCU2 observations of Cen A. The 2009 January and February observations using the `SkyVLE` background required positive corrections of a few percent. Figure 2 shows the values of the background correction factor for the 13 observation intervals and the 47 daily data sets for both PCU2 and HEXTE. The corrections for the two different PCU2 background estimations are quite different.

4. RESULTS

4.1. The Energy Spectrum of Cen A

All data were fitted with a model representing redshifted line-of-sight absorption (`XSPEC` model `ZPHABS`) with abundances set to those of Wilms et al. (2000) and utilizing the Verner et al. (1996) cross sections, a power law (`XSPEC` model `PEGPWRLW`) with a normalization equal to the unabsorbed flux in the 2–10 keV range, and a redshifted Gaussian component representing iron Kα emission with width set to the *Suzaku* value of 30 eV (Markowitz et al. 2007). Instrumental line-like residuals near 4.5, 8.0, and 29 keV, when present, were fit as Gaussians as part of the model. Including one or more of these Gaussians

[7] http://heasarc.gsfc.nasa.gov/docs/xanadu/xspec/manual/XSmodelRecorn.html

Table 2
Best-fit Parameters for the 13 Observations of Cen A with *RXTE*

Date	N_H[a]	Γ[b]	Norm(2–10)[c]	E(Fe Kα)[d]	Flux(Fe Kα)[e]	EW(Fe Kα)[f]	χ^2/dof[g]	χ^2_ν
1996 Aug	$15.8^{+0.8}_{-0.7}$	$1.824^{+0.028}_{-0.027}$	$333.1^{+8.7}_{-8.3}$	$6.44^{+0.06}_{-0.05}$	$5.14^{+0.63}_{-0.63}$	155^{+40}_{-35}	135.8/118	1.15
1998 Aug	$14.3^{+0.3}_{-0.3}$	$1.829^{+0.011}_{-0.011}$	$305.4^{+3.1}_{-3.1}$	$6.40^{+0.03}_{-0.02}$	$4.40^{+0.24}_{-0.24}$	141^{+14}_{-12}	141.2/119	1.19
2000 Jan	$15.6^{+0.4}_{-0.4}$	$1.834^{+0.014}_{-0.013}$	$513.1^{+6.8}_{-6.6}$	$6.40^{+0.05}_{-0.06}$	$4.39^{+0.50}_{-0.50}$	84^{+17}_{-14}	118.3/118	1.00
2003 Mar[h]	$22.7^{+0.2}_{-0.2}$	$1.799^{+0.007}_{-0.007}$	$711.8^{+5.0}_{-4.2}$	$6.32^{+0.03}_{-0.03}$	$4.72^{+0.37}_{-0.37}$	63^{+9}_{-8}	118.3/117	1.01
2004 Jan[i]	$25.7^{+0.3}_{-0.3}$	$1.787^{+0.010}_{-0.010}$	$422.5^{+3.9}_{-3.9}$	$6.43^{+0.03}_{-0.02}$	$5.67^{+0.30}_{0.30}$	140^{+11}_{-11}	144.9/116	1.25
2004 Feb[h]	$24.2^{+0.4}_{-0.4}$	$1.796^{+0.013}_{-0.014}$	$478.6^{+5.7}_{-6.3}$	$6.39^{+0.03}_{-0.04}$	$5.15^{+0.44}_{-0.45}$	106^{+14}_{-14}	125.2/117	1.07
2005 Aug	$19.4^{+0.8}_{-0.8}$	$1.848^{+0.027}_{-0.027}$	$408.5^{+10.9}_{-10.5}$	$6.41^{+0.11}_{-0.10}$	$3.17^{+0.77}_{-0.77}$	79^{+28}_{-29}	96.4/118	0.82
2005 Dec	$18.2^{+0.6}_{-0.6}$	$1.823^{+0.022}_{-0.023}$	$301.5^{+6.7}_{-6.4}$	$6.32^{+0.06}_{-0.06}$	$3.51^{+0.47}_{-0.48}$	112^{+25}_{-23}	105.9/118	0.90
2006 Jul	$18.8^{+0.4}_{-0.4}$	$1.844^{+0.013}_{-0.013}$	$544.5^{+6.8}_{-6.9}$	$6.34^{+0.05}_{-0.05}$	$4.21^{+0.51}_{-0.50}$	77^{+15}_{-14}	107.3/118	0.91
2006 Dec[h]	$18.7^{+0.3}_{-0.3}$	$1.832^{+0.012}_{-0.011}$	$402.7^{+4.5}_{-4.6}$	$6.37^{+0.03}_{-0.04}$	$4.46^{+0.33}_{-0.33}$	109^{+13}_{-13}	134.4/117	1.15
2007 Aug[h]	$17.3^{+0.2}_{-0.3}$	$1.818^{+0.009}_{-0.009}$	$736.4^{+6.5}_{-6.4}$	$6.30^{+0.05}_{-0.05}$	$4.27^{+0.51}_{-0.50}$	56^{+11}_{-11}	129.2/117	1.10
2009 Jan	$17.0^{+0.2}_{-0.1}$	$1.826^{+0.005}_{-0.006}$	$985.8^{+5.1}_{-5.0}$	$6.29^{+0.03}_{-0.04}$	$5.01^{+0.40}_{-0.40}$	49^{+6}_{-7}	137.1/118	1.16[j]
2009 Feb	$17.9^{+0.2}_{-0.2}$	$1.830^{+0.008}_{-0.007}$	$992.3^{+7.5}_{-7.5}$	$6.28^{+0.04}_{-0.05}$	$4.81^{+0.59}_{-0.59}$	46^{+10}_{-8}	134.2/118	1.14

Notes.
[a] Inferred line-of-sight equivalent hydrogen column density (10^{22} cm^{-2}).
[b] Power-law photon index.
[c] Power-law normalization (2–10 keV; 10^{-12} erg cm^{-2} s^{-1}).
[d] The line energy (keV).
[e] The line flux (10^{-4} Photons cm^{-2} s^{-1}).
[f] The line equivalent width (eV); uncertainties are 99% confidence.
[g] Total chi-squared/degrees of freedom.
[h] Additional systematics line at 29.5 keV included in the fit.
[i] Additional systematics lines at 4.5 and 29.5 keV included in the fit.
[j] A single PCU2 bin contributed $\chi^2 = 21$; without it, $\chi^2 = 113.1/117 = 0.97$.

Table 3
Fluxes and Limits on Reflection and Cutoffs for the 13 Observations of Cen A with *RXTE*

Date	Flux (1 keV)[a]	Flux (2–10 keV)[b]	Flux (20–100 keV)[b]	Γ	E_{cut}[c]	χ^2_ν	R[d]	χ^2_ν
1996 Aug	$0.099^{+0.007}_{-0.009}$	$1.857^{+0.007}_{-0.007}$	$4.99^{+0.19}_{-0.18}$	$1.759^{+0.058}_{-0.092}$	154^{+539}_{-86}	1.12	$\leqslant$8.7	1.16
1998 Aug	$0.092^{+0.002}_{-0.003}$	$1.773^{+0.003}_{-0.002}$	$4.54^{+0.06}_{-0.06}$	$1.804^{+0.015}_{-0.027}$	$\geqslant$204	1.17	$\leqslant$2.1	1.20
2000 Jan	$0.155^{+0.005}_{-0.005}$	$2.843^{+0.005}_{-0.006}$	$7.52^{+0.08}_{-0.11}$	$1.832^{+0.014}_{-0.018}$	$\geqslant$689	1.01	$\leqslant$7.9	1.01
2003 Mar	$0.203^{+0.004}_{-0.003}$	$3.351^{+0.002}_{-0.003}$	$11.23^{+0.07}_{-0.07}$	$1.796^{+0.007}_{-0.006}$	$\geqslant$1399	1.03	$\leqslant$4.9	1.01
2004 Jan	$0.120^{+0.002}_{-0.003}$	$1.909^{+0.002}_{-0.002}$	$7.01^{+0.08}_{-0.05}$	$1.765^{+0.015}_{-0.015}$	607^{+747}_{-225}	1.00	$\leqslant$1.0	1.27
2004 Feb	$0.136^{+0.005}_{-0.004}$	$2.207^{+0.004}_{-0.003}$	$7.63^{+0.07}_{-0.09}$	$1.793^{+0.013}_{-0.021}$	$\geqslant$693	1.07	$\leqslant$4.4	1.08
2005 Aug	$0.126^{+0.005}_{-0.008}$	$2.048^{+0.007}_{-0.007}$	$5.78^{+0.14}_{-0.12}$	$1.845^{+0.031}_{-0.049}$	$\geqslant$318	0.82	$\leqslant$18.2	0.82
2005 Dec	$0.090^{+0.004}_{-0.005}$	$1.579^{+0.005}_{-0.004}$	$4.55^{+0.11}_{-0.11}$	$1.816^{+0.027}_{-0.049}$	$\geqslant$209	0.92	$\leqslant$12.6	0.91
2006 Jul	$0.167^{+0.005}_{-0.005}$	$2.767^{+0.003}_{-0.004}$	$7.79^{+0.11}_{-0.12}$	$1.842^{+0.012}_{-0.016}$	$\geqslant$814	0.92	$\leqslant$8.2	0.92
2006 Dec	$0.121^{+0.004}_{-0.003}$	$2.071^{+0.002}_{-0.003}$	$5.89^{+0.10}_{-0.09}$	$1.809^{+0.026}_{-0.025}$	$\geqslant$242	1.12	$\leqslant$7.1	1.14
2007 Aug	$0.216^{+0.005}_{-0.004}$	$3.887^{+0.004}_{-0.003}$	$11.11^{+0.10}_{-0.11}$	$1.815^{+0.009}_{-0.013}$	$\geqslant$878	1.11	$\leqslant$5.7	1.10
2009 Jan	$0.293^{+0.004}_{-0.003}$	$5.236^{+0.003}_{-0.003}$	$14.68^{+0.10}_{-0.09}$	$1.823^{+0.006}_{-0.004}$	$\geqslant$2796	1.21	$\leqslant$4.6	1.16
2009 Feb	$0.297^{+0.006}_{-0.005}$	$5.139^{+0.003}_{-0.005}$	$14.60^{+0.12}_{-0.11}$	$1.828^{+0.008}_{-0.008}$	$\geqslant$2499	1.17	$\leqslant$3.9	1.15

Notes.
[a] Power-law normalization at 1 keV (photons cm^{-2} s^{-1} keV^{-1}).
[b] Flux in units of 10^{-10} erg cm^{-2} s^{-1}.
[c] Exponential cutoff energy (keV).
[d] Compton reflection strength (%).

did not significantly affect the best-fit parameters of the rest of the model, but did reduce χ^2 nearer to 1 in most cases.

The best-fit spectral parameters for the power-law fit to the 13 observation intervals are given in Table 2 and the 2–10 keV and 20–100 keV fluxes are given in Table 3. In order for comparisons to spectra modeled with the XSPEC model POWERLAW, the best-fit flux at 1 keV is also given in Table 3 for additional fitting done with the POWERLAW model component replacing the PEGPWRLW description of the power law. We achieved good fits with both versions of this model in all cases.

A second model was tested with the power law replaced with the XSPEC model CUTOFFPL, which is a power-law times an exponential to approximate any rollover of the spectrum due to Comptonization processes. This second model did not result in significantly lower χ^2 values in any case, and since it contained an added parameter (the cutoff energy), we used the results

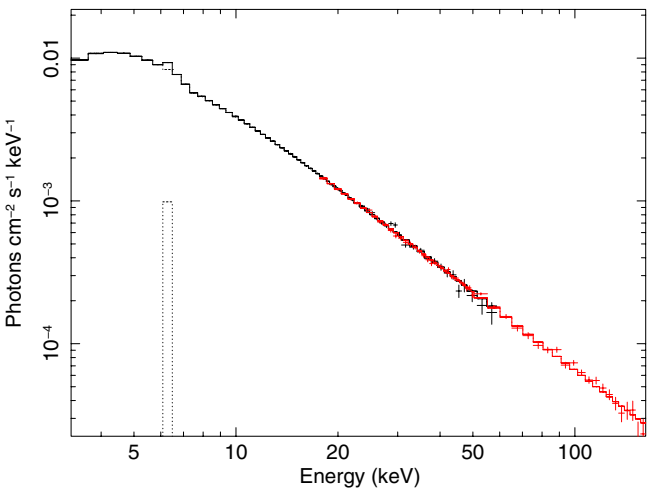

Figure 3. Inferred incident spectrum of the 2009 January set of observations. PCU2 top layer 3–60 keV and HEXTE 18–200 keV data points are shown along with the model of a single absorbed power law with an iron emission line at 6.4 keV. The line component is indicated by the dotted lines.

(A color version of this figure is available in the online journal.)

from the pure power-law fits in the discussions that follow. Lower limits, and in two cases best-fit values, to the rollover energy are given in Table 3 for comparison to such fits by other authors. The two observations yielding best-fit values of the rollover energy have a common range of 382 keV–693 keV. This is consistent with the Rivers et al. (2011) lower limit of 490 keV from fitting the sum of all the Cen A data. The observations with the strongest lower limits to the cutoff energy ($\geqslant$2796 keV and $\geqslant$2499 keV), however, occur at the highest flux values in 2009. This latter result is strong evidence for no cutoff being necessary, as measured over the 3–200 keV band (Figure 3). Future instrumentation with good sensitivity to hundreds of keV acquired over a realistic amount of observing time will be required to derive a meaningful value for the rollover energy, if indeed that is the proper description of the high-energy spectrum of Cen A.

A third model included the XSPEC model PEXRAV component of Compton reflection from cold/neutral material in a semi-infinite slab (i.e., from the accretion disk; Magdziarz & Zdziarski 1995) along with the observed power law. The folding energy was set to 1000 keV and the inclination angle was fixed at 62.°6 (Burtscher et al. 2010) from the dust emission in the mid-infrared. This model also did not improve the fit over a single power law, but did provide upper limits on the reflection component (Table 3). All upper limits were consistent with the Rivers et al. (2011) upper limit of 0.5% from a similar fit to the entire Cen A set of observations.

4.1.1. Time Average Cen A Spectra

In order to set the stage for studying spectral variability of Cen A in the next section, we present the results of a separate study of the time-averaged spectra of 23 bright active galaxies observed by *RXTE* over the duration of the *RXTE* mission (Rivers et al. 2011). In the case of Cen A, the time average spectrum included all of the observations through 2009 February. Rivers et al. (2011) found a mean Cen A power-law index $\Gamma = 1.83 \pm 0.01$, a mean $N_{\rm H} = (1.69 \pm 0.03)\times 10^{23}$ cm^{-2}, a mean iron line energy of 6.38 ± 0.09 keV, and a mean iron line flux of $(4.9 \pm 0.7) \times 10^{-4}$ photons cm^{-2} s^{-1}. The upper limit to a Compton reflection component was $R < 0.5\%$, and the lower limit to the high-energy rollover was >490 keV. As will be demonstrated below, these values are consistent with the mean values found by averaging the 13 observation intervals, i.e., a mean power-law index of 1.822 ± 0.004, a mean iron line energy of 6.361 ± 0.014 keV, and a mean iron line flux of $(4.55 \pm 0.14) \times 10^{-4}$ photons cm^{-2} s^{-1}.

4.2. Spectral Variability

4.2.1. Months to Years

Individual Cen A observations spanned intervals from less than 1 ks to a few hours, with separations between observations of days to 3 years. Consequently, the spectral analysis could be performed on a range of temporal scales. As will be shown, the best-fit parameters of the day-to-day observations did not show large variability and thus only the best-fit parameters from the 13 observational intervals are given in Table 2. Figures 4–8 display the 13 sets of best-fit spectral parameters for the observation intervals on the left and those from fitting the individual days on the right. Figure 4 shows the best-fit unabsorbed power-law 2–10 keV flux, column density, and power-law index; Figure 5 shows the best-fit iron line energy, flux, and equivalent width, and Figure 6 shows the 2–10 keV and 20–100 keV total fluxes from Cen A.

The inferred line-of-sight column density experienced nearly a factor of two in variability, with an interval of high density in the 2003 March to 2004 February data and lower density otherwise. The power-law index remained essentially constant ($\Gamma = 1.822 \pm 0.004$) over 12.5 years, with a slight ($\sim$2%) reduction at the time of the increased column density. The best-fit iron line energy values (6.361 ± 0.014 keV) were consistent with fluorescence of cold/neutral material at 6.4 keV, and the iron line flux appears to vary minimally over the observing decade with a mean value of 4.55 ± 0.14 photons cm^{-2} s^{-1}. The equivalent width of the iron emission ranged from 46^{+10}_{-8} to 155^{40}_{-35} eV, and the variation was as expected for a constant flux and varying power-law continuum responsible for the fluorescing flux.

Figure 7 (top) shows the values of the iron line flux plotted versus the power-law normalization for the 13 observing intervals (left) and the 47 daily measurements (right). The average iron line flux is given by the horizontal line indicating no overall dependence of the iron line flux with the power-law normalization. Similarly, the power-law index showed no systematic variation with an instantaneous power-law flux (Figure 7, bottom). The very sparse sampling of the *RXTE* observations over 12.5 years prevented a meaningful conclusion vis-à-vis the relation between the power-law emission and fluorescent iron line fluxes, i.e., any time delay between power-law and iron line fluxes.

Figure 8 (top) shows the variations in the iron line flux versus column depth for the 13 observing intervals and for the daily observations, while Figure 8 (bottom) displays the equivalent width of the iron line versus column depth. Figure 9 shows that the equivalent width of the iron line is inversely correlated with the power-law flux, which is to be expected if the iron line flux is essentially constant with varying power-law flux. Figure 10 reveals that there is no temporal correlation of the iron line with either the 2–10 keV power-law flux or the column density. In addition, Figure 10 (bottom) plots the measured column density versus the measured power-law flux, clearly showing that no correlation exists between these two parameters also. Hence, we find no correlations between any of the spectral parameters,

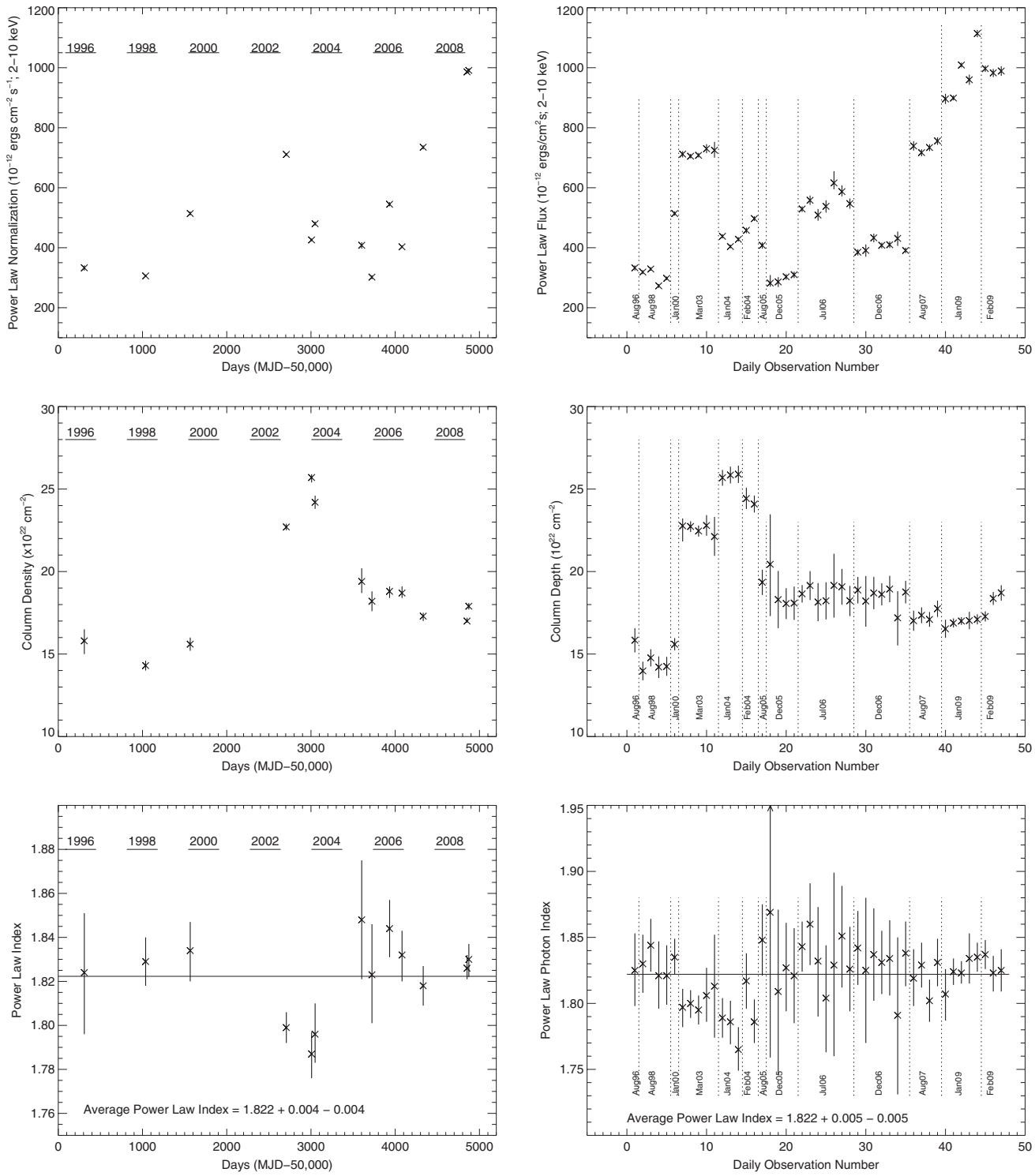

Figure 4. Best-fit 2–10 keV normalizations of the power-law (top), low-energy absorption (middle), and power-law photon indices (bottom) for the 13 observation intervals (left) and the 47 daily spectra (right). Years and observing intervals are shown. Average values plus 90% uncertainties are given for the power-law index. Error bars represent 90% uncertainties.

other than the anti-correlation of equivalent width of the iron line and unabsorbed power-law flux.

4.2.2. Day to Day

We have combined data from individual ObsIDs to produce 47 daily spectra from 1996 August 8 to 2009 February 21. As can be seen in Table 4, several sets of one or more contiguous days are present. The data from late 2009 January 15 and early January 16 have been combined into a single day since the data are effectively contiguous. Similarly the data for 2009 January 18, 19, and 20 have been combined, as well as 2009 January 25, 26, 27, 28. From these data sets, we can derive indications of the variations from day to day exhibited by Cen A. Additionally, one can compare spectral parameters from observations a few days apart.

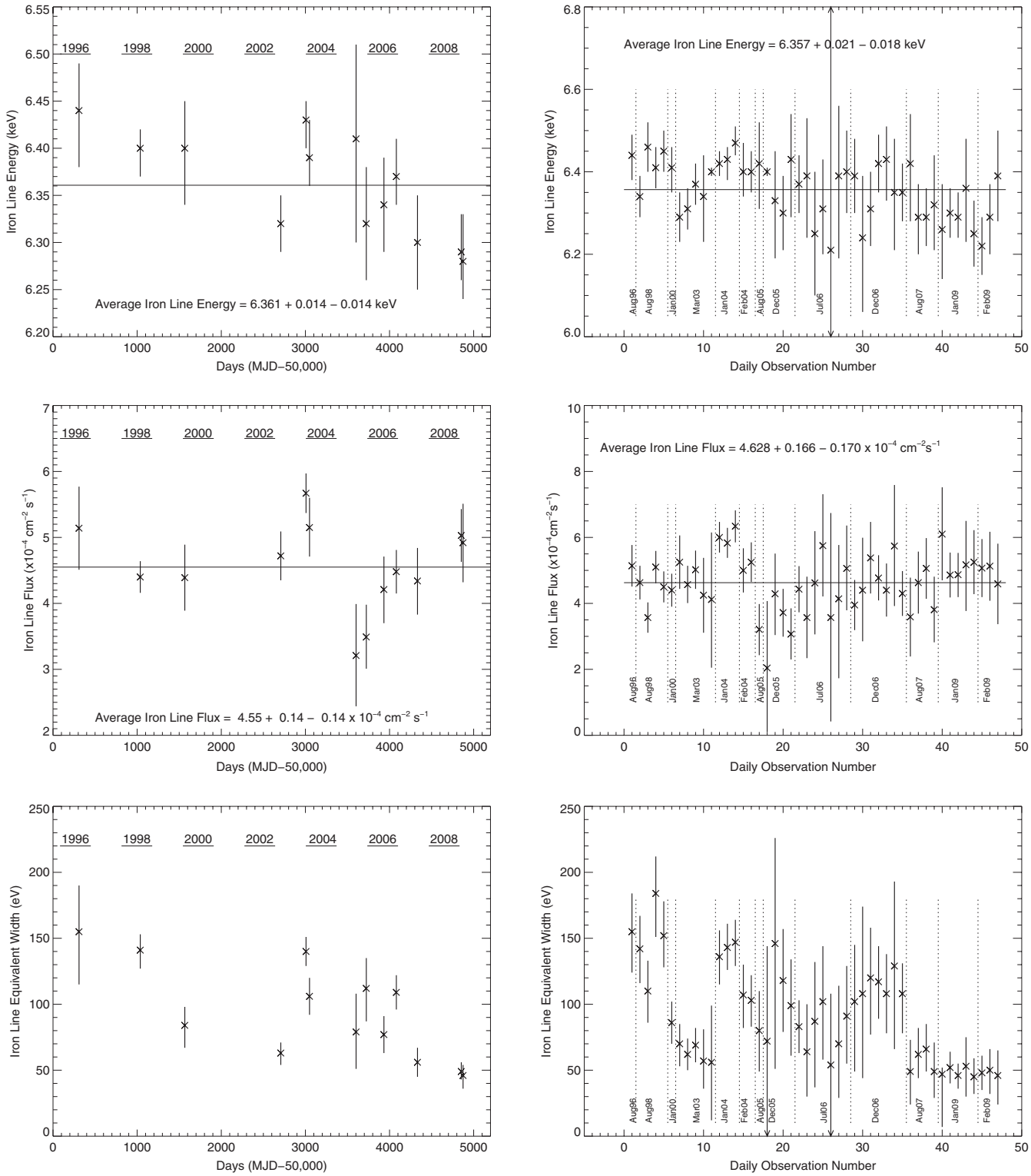

Figure 5. Best-fit iron line energy (top), iron line flux (middle), and equivalent width (bottom) spectral parameters resulting from fitting the 13 separate observation interval spectra and the 47 daily spectra. Error bars represent 90% uncertainties. Average values plus 90% uncertainties are given for the iron line energy and flux. Years and observing intervals are shown.

Column density $N_{\rm H}$. Figure 4 (middle/right panel) shows the best-fit values of $N_{\rm H}$ for each of the 47 daily spectra with the 13 observational intervals indicated. Significant variations in $N_{\rm H}$ are not seen on a day-to-day scale. The change over the three weeks between 2009 February 2 and 20 represents a 6% rise, while the interval from 2004 January 4 to February 13 had a 6% drop in column density over 40 days. On the eight month timescale, a drop of 10% is seen from 2006 December 15 to 2007 August 18.

Power-law photon index Γ. The value of the power-law index was clearly below average in 2003 and early 2004 (Figure 4, bottom/right panel). This decrement amounts to only 2%, however.

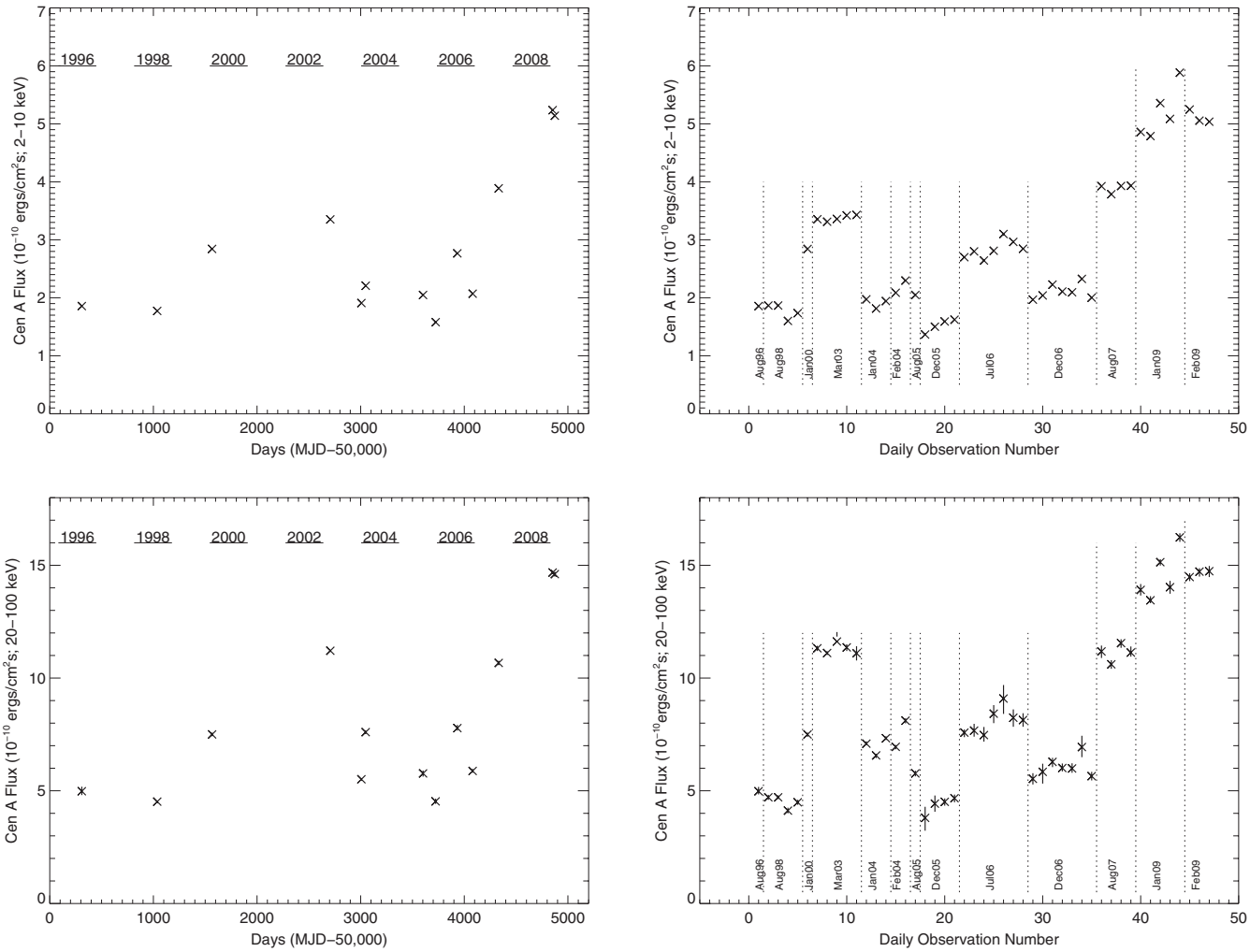

Figure 6. *RXTE* Cen A 2–10 keV (top) and 20–100 keV (bottom) fluxes for the 13 observation intervals and the 47 daily spectra. Years and observing intervals are shown. Error bars representing 90% uncertainties are generally smaller than the symbols.

Table 4
Start/Stop Times for the 51 PCU2 Light Curves of Cen A

Obs. Interval	Date	Time (UT)	Obs. Interval	Date	Time (UT)	Obs. Interval	Date	Time (UT)
1996 Aug	8/14	2:43–8:03	2005 Dec	12/16	0:08–0:21	2007 Aug	8/18	3:54–23:27
1998 Aug	8/9	1:24–23:56		12/17	17:06–22:09		8/19	0:19–15:03
	8/10	0:01–7:18		12/20	20:00–24:07		8/20	14:10–24:07
	8/14	3:08–23:58		12/23	0:08–22:52		8/22	3:44–7:51
	8/15	0:02–8:57	2006 Jul	7/13	10:08–24:27	2009 Jan	1/15	20:34–23:58
2000 Jan	1/23	7:38–23:24		7/14	11:03–22:28		1/16	0:02–19:20
2003 Mar	3/7	12:02–20:58		7/16	17:56–23:04		1/18	22:24–23:58
	3/8	1:04–17:28		7/17	0:13– 17:43		1/19	0:02–23:58
	3/9	3:33–18:48		7/18	10:54–12:38		1/20	0:02–1:57
	3/10	8:00–16:02		7/19	13:32–16:54		1/25	22:19–23:58
	3/11	7:43–8:17		7/20	11:39–22:55		1/26	0:02–0:44
2004 Jan	1/2	8:56–23:58	2006 Dec	12/8	7:03–13:45		1/27	18:16–23:49
	1/3	0:03–23:47		12.9	1:39–2:21		1/28	0:32–1:23
	1/4	0:46–16:29		12/10	1:47–9:26	2009 Feb	2/2	13:58–22:39
2004 Feb	2/13	9:41–16:46		12/11	4:26–16:19		2/20	4:59–19:19
	2/14	9:19–19:39		12/12	9:39–13:12		2/21	4:06–7:53
2005 Aug	8/20	3:59–7:58		12/13	9:09–19:14			
				12/15	5:10–18:19			

Power-law flux. The unabsorbed power-law 2–10 keV flux is seen to vary with the observational interval fluxes (Figure 4, top/right panel) in general. Within each interval, the daily values remain relatively constant, except for the 2009 January interval where the flux increased by about 20% with the power-law index remaining constant. This variability is

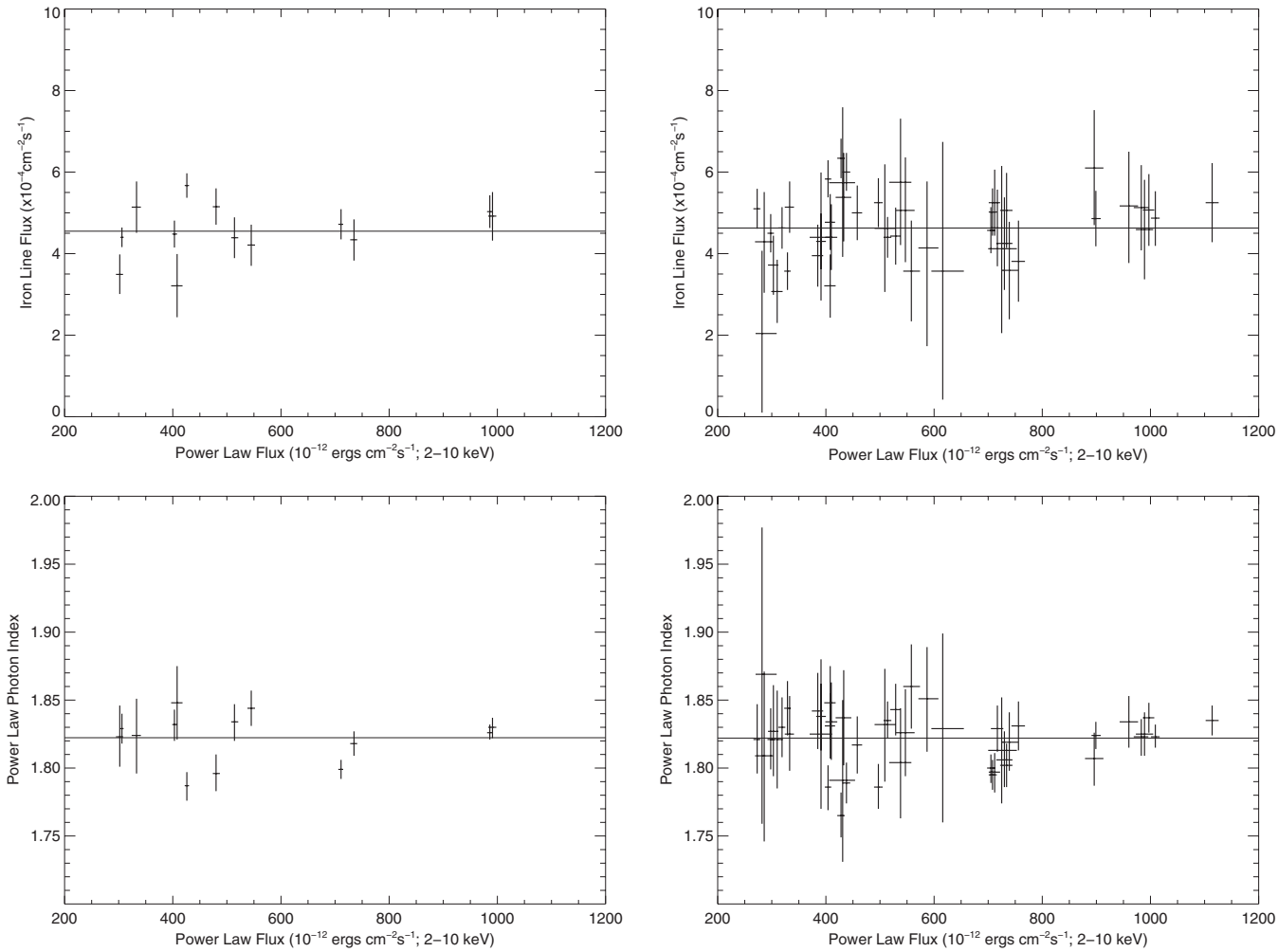

Figure 7. Iron line flux (top) and power-law index (bottom) as a function of the unabsorbed power-law flux for the 13 observation intervals (left) and 45 daily spectra (right). The average iron line flux (top) and the average power-law index (bottom) are shown as horizontal lines. Error bars represent 90% uncertainties.

seen in both the 2–10 keV and 20–100 keV fluxes (Figure 6), thus indicating that the power-law intensity is the variable and not the power-law index or absorbing column. The lack of a correlation between the absorbing column density and the unabsorbed power-law flux is clearly demonstrated in Figure 10 (bottom).

Iron line. The iron line centroid, flux, and equivalent width for each daily observation are shown in the right-hand panels of Figure 5. The 2004 January values of the centroid are barely 1% above the average, while the flux is ∼30% above the mean. While this is simultaneous with the highest value of $N_{\rm H}$ and the 2% drop in the power-law index, it is not considered significant when the overall variations are taken into account (see Figure 10).

From this we can conclude, as with the 13 observational intervals, the Cen A spectrum only varies in power-law normalization and column density, with relatively small variations in individual spectral parameters beyond that. Sustained monitoring at regular intervals over several months would be necessary for possible reverberation mapping of the iron line emitting material and for detailed studies of the variation in column density with respect to a clumpy torus model. Such monitoring by *RXTE* began in 2010 January and continues at present.

4.3. Temporal Variability

4.3.1. Light Curves

The PCU2 light curves of the first six observations (1996 August to 2004 February) were originally published in Rothschild et al. (2006), and the revised light curves for all observations are given here, reflecting improvements in the PCA response and background estimation since then. Background-subtracted light curves with 256 s time bins over the complete PCU2 energy band (2–60 keV) were generated for the 53 days with four or more time bins. In three cases, observations overlapped slightly into the next day, and this is indicated in Table 4 (which gives the start and stop times of each daily light curve) by stop times greater than 24 hr. The resulting 51 light curves are plotted versus time since the time of the first temporal bin (Figure 11). The short gaps in the light curves are the result of Earth occultations and passages through the SAA, while longer gaps and multiple day observations are the result of *RXTE* scheduling of other observations with higher priority. Also shown on the daily light curve figures are the average rate for the associated observation interval (dashed line) and the ±10% rates (dot-dash lines).

It is clear from the figures that Cen A varies by ±10% quite regularly over a week's time, with some variations occurring on

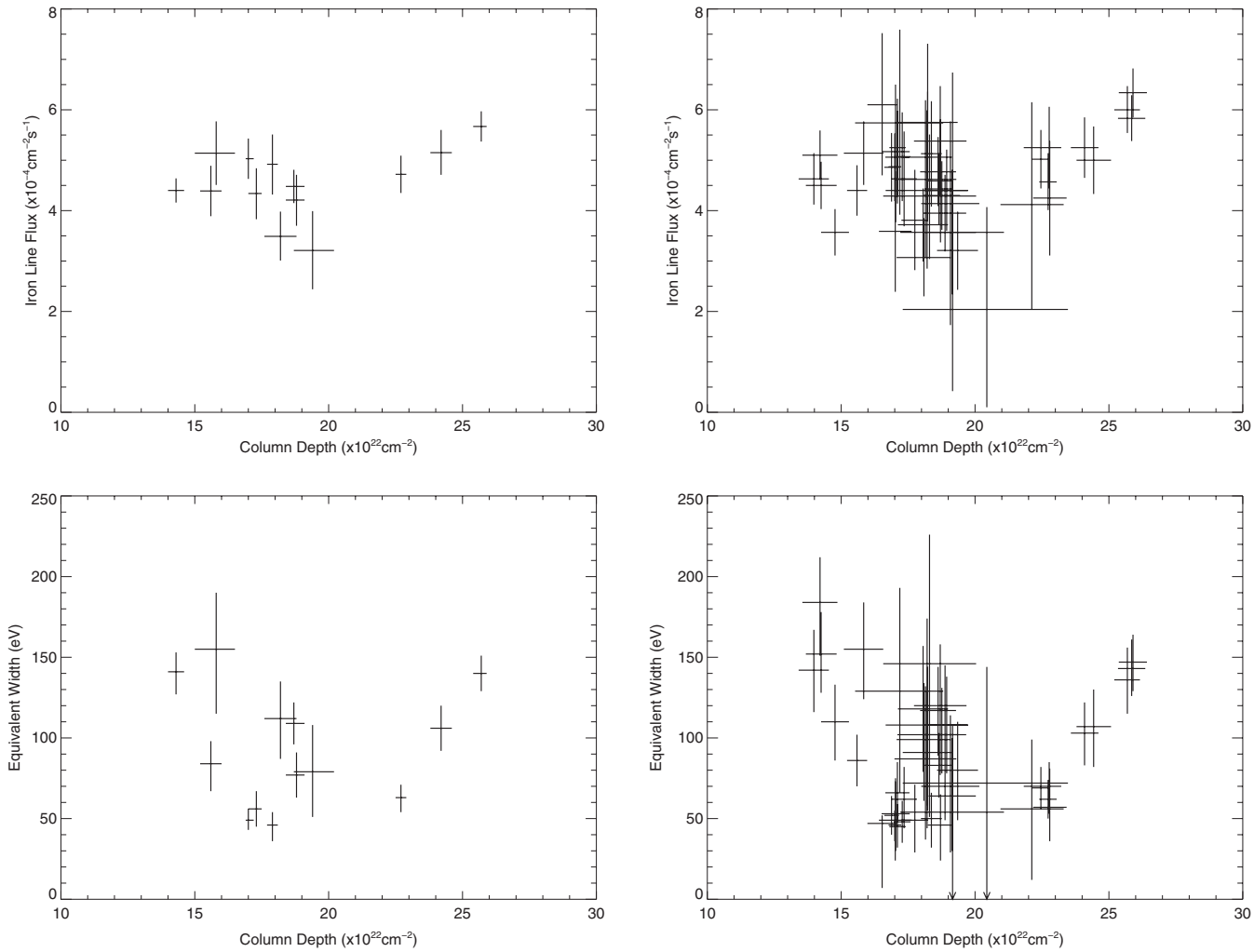

Figure 8. Iron line flux as a function of the low-energy column depth (top) and the iron line equivalent width as a function of the column depth (bottom) for the 13 observation intervals (left) and 47 daily spectra (right). Error bars represent 90% uncertainties.

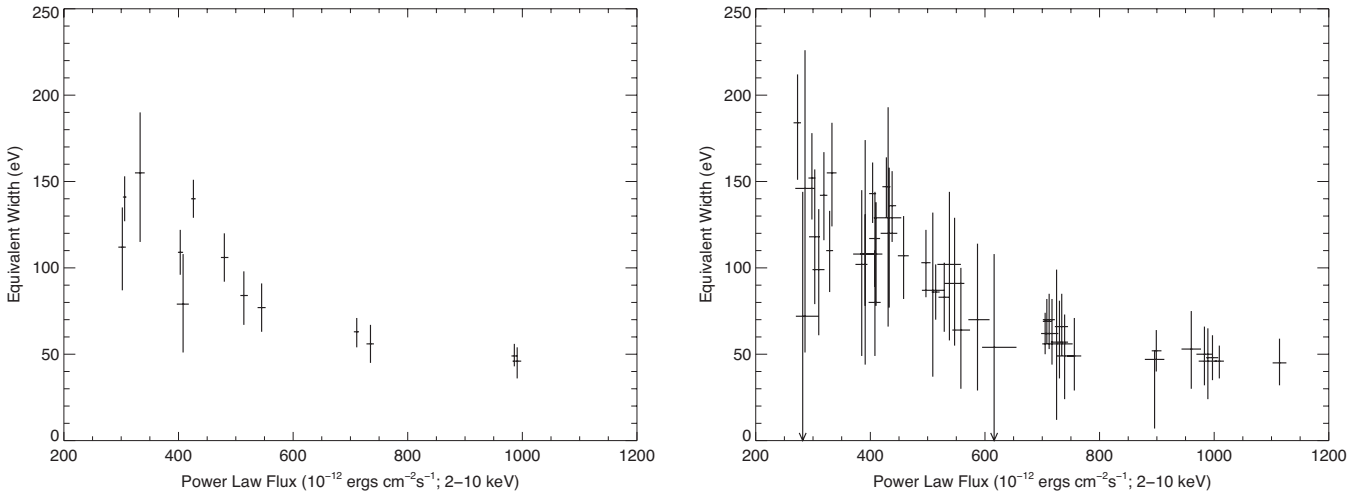

Figure 9. Equivalent width of the iron line is presented as a function of the unabsorbed power-law 2–10 keV flux. The anti-correlation between the two parameters is clear, which indicates that the iron line was not responding to the power-law continuum on the timescales available.

a daily timescale. This is especially clear in the 2004 January 2–4 and 2004 February 13–14 light curves. A 5% change over a few hours was seen between the end of 2006 December 12 and the beginning of December 13.

4.3.2. Power Spectral Density Function

In this section, we present the broadband PSD analysis for Cen A by combining data from three X-ray instruments. While

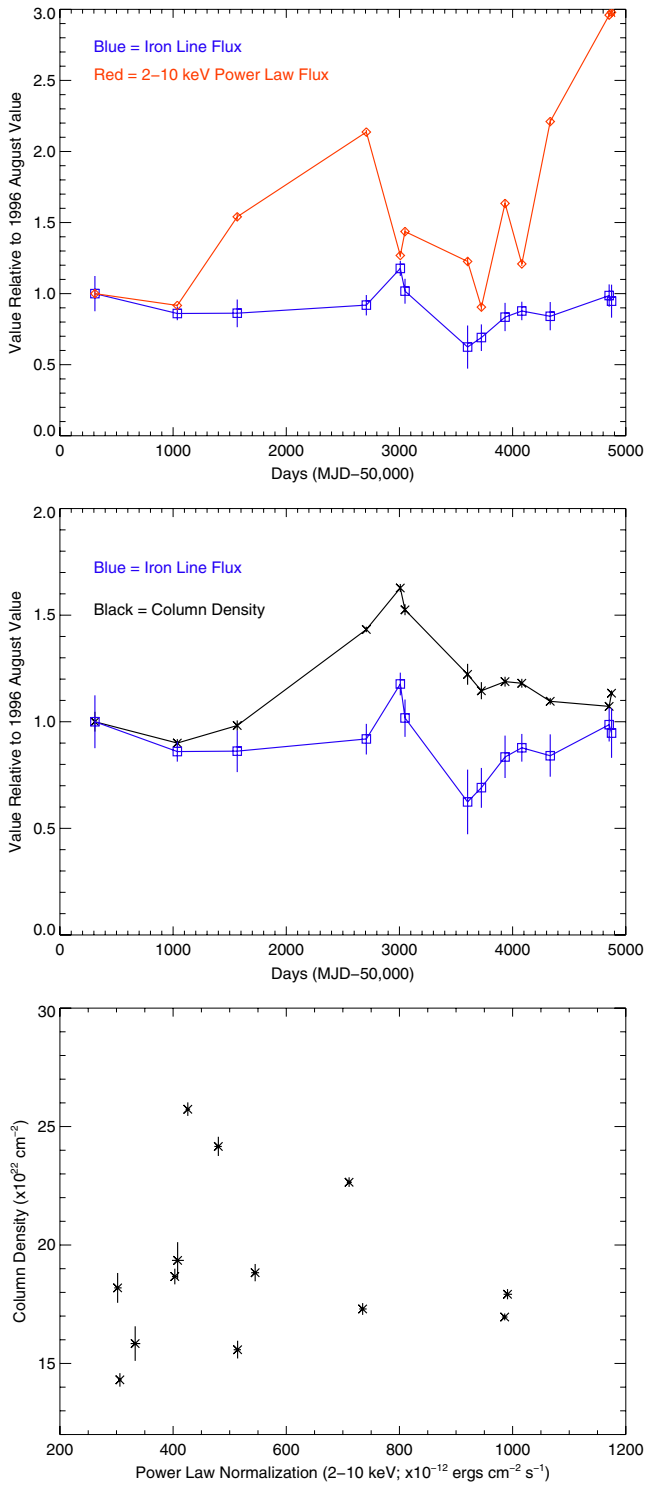

Figure 10. Variation in the iron line flux and the 2–10 keV unabsorbed power-law flux (top) and the column density and the iron line flux (middle) as a function of time. The values are normalized to the first observation in 1996 August. The lack of correlation is clear in both plots. The column density as a function of the power-law flux (bottom) shows no correlation between the two parameters.

(A color version of this figure is available in the online journal.)

the resulting PSD does not have the same temporal frequency coverage as those for many previously measured Seyferts, we were still able to derive a break in the power spectrum and demonstrate that the PSD shape was similar to those seen in both Seyferts and X-ray black hole binaries.

To facilitate PSD analysis and allow use of the Discrete Fourier Transform (DFT) (Oppenheim & Schafer 1975), we used only light curves which are evenly spaced and relatively continuous (no large gaps). As shown below, for Cen A, we combined data from *RXTE*/ASM, *RXTE*/PCA, and *XMM-Newton* to probe low-, medium-, and high-temporal frequencies, respectively.

The sampling obtained by *RXTE*/PCA was relatively inhomogeneous, and we found only one "high-quality" PCA light curve which, after binning on the satellite orbital timescale, would make using analysis via a DFT straightforward: that from the 2004 January 2–4 observation. These data were obtained from observation IDs 70152-01-01-14, 70152-01-02-000, 70152-01-02-010, and 70152-01-02-[00-16]; the resulting light curve, binned to the satellite orbital timescale of 5.7 ks, yielded a light curve with only 3/36 points missing. With a duration of 2.2 days, we were able to probe variability on temporal frequencies near 10^{-5}–10^{-4} Hz.

RXTE is in a low-Earth orbit, and the resulting Earth occultation of the PCA every ∼6 ks severely complicates PSD analysis for temporal frequencies above $1/(2 \times 6\,\mathrm{ks})$. For the high-temporal frequency PSD (10^{-4}–10^{-3} Hz), we relied on the uninterrupted light curves provided by *XMM-Newton* EPIC pn. *XMM-Newton* observed the nucleus of Cen A twice, once in 2001 February for a duration of 23.4 ks (good exposure time 19.4 ks after screening) and again in 2002 February for a duration of 15.3 ks (good exposure time 8.9 ks). We used the longer duration 2001 data (ObsID 0093650201; data obtained from the HEASARC public archive), which used the medium filter. Using `XSELECT` version 2.4a, we extracted 2–10 keV source and background light curves. We used only PATTERN = 0 events to reduce the impact of pile-up. The source region was a circle of radius 40″ centered on the source; the background was extracted from an identical size circle ∼3′ away on the same CCD chip. We also extracted and inspected the 10–13 keV pn background light curve for flares, but found none. The light curves were binned to 300 s; variability at shorter timescales was dominated by Poisson noise.

The decade-long light curve from pointed PCA observations is too gap dominated for reliable PSD analysis using a DFT, and so we rely on the light curve from the ASM. We downloaded 1 day averaged sum-band (1.5–12 keV) light curves from the MIT ASM database (http://xte.mit.edu), obtained between MJD 50087−54976. We removed those few 1 day data points which had negative fluxes or uncertainties greater than the average flux value, and binned the light curve to 20 days; power at temporal frequencies higher than $\sim 1/(2 \times 20\mathrm{d})$ was dominated by power due to Poisson noise and systematics associated with background subtraction, source confusion, etc. PSD measurements using 1 and 5 day binned light curves allowed us to empirically determine this level of power, P_{Psn}; fitting a constant to the binned PSD above $10^{-6.6}$ Hz yielded $P_{\mathrm{Psn}} = 33100\ \mathrm{Hz}^{-1}$.

Periodograms were measured for each light curve separately, binned into a PSD, and then the three PSD segments were combined (e.g., Edelson & Nandra 1999). Due to PSD measurement distortion effects (namely, aliasing, which affects only the PCA light curve, and red-noise leakage), the model-dependent Monte Carlo method described by Uttley et al. (2002) was used to assign proper uncertainties to each binned PSD point and determine the intrinsic, underlying PSD shape. The reader is referred to Uttley et al. (2002) for the definitions of the χ^2_{dist}

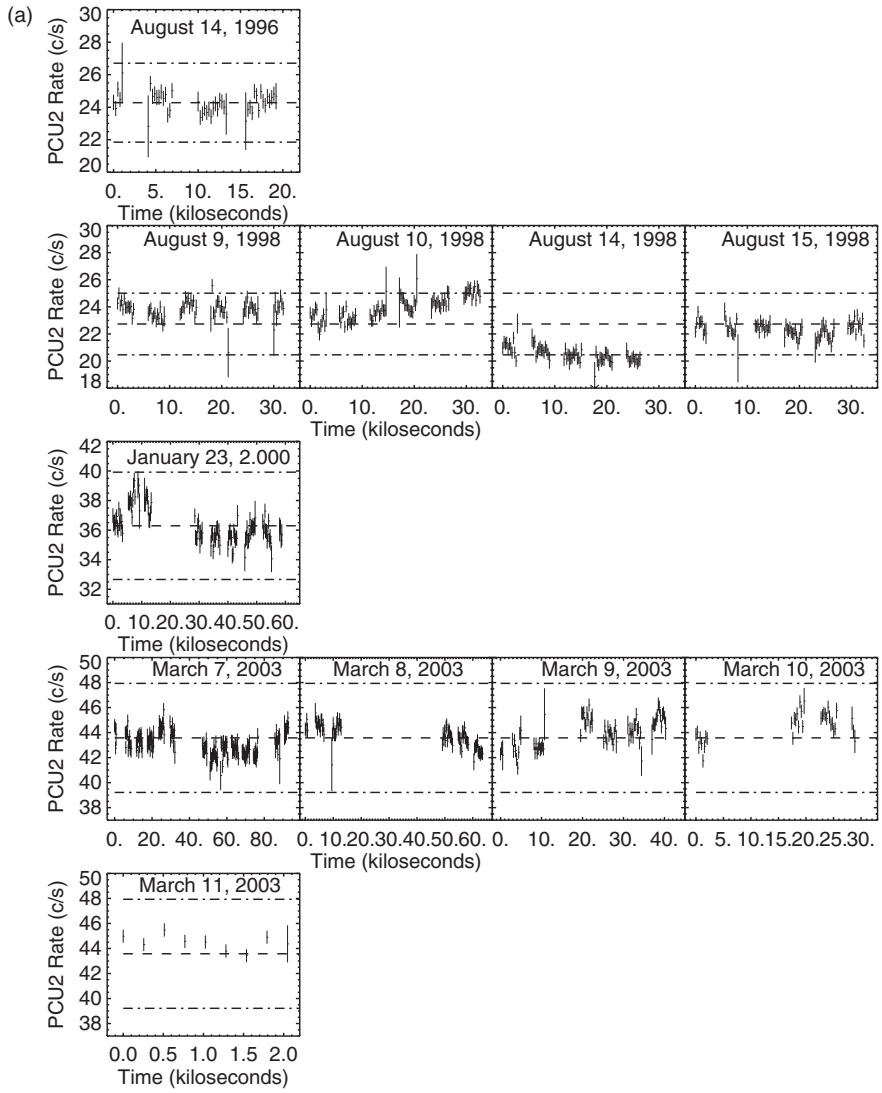

Figure 11. (a) Daily light curves of Cen A with 256 s time bins over the full PCU2 energy range for observation intervals 1996 August, 1998 August, 2000 January, and 2003 March. The dashed line is the average rate for the observational interval and the dash-dot lines represent ±10% in the rate. (b) Daily light curves of Cen A with 256 s time bins over the full PCU2 energy range for observation intervals 2004 January, 2004 February, 2005 August, and 2005 December. The dashed line is the average rate for the observational interval and the dash-dot lines represent ±10% in the rate. (c) Daily light curves of Cen A with 256 s time bins over the full PCU2 energy range for observation intervals 2006 July, 2006 December, and 2007 August. The dashed line is the average rate for the observational interval and the dash-dot lines represent ±10% in the rate. (d) Daily light curves of Cen A with 256 s time bins over the full PCU2 energy range for observation intervals 2009 January and 2009 February. The dashed line is the average rate for the observational interval and the dash-dot lines represent ±10% in the rate.

statistic used to compare observed and modeled PSDs and the rejection probability used to determine goodness of fit of model PSD shapes tested.

Initial PSD construction closely followed Section 3.1 of Markowitz et al. (2003). Light curves were linearly interpolated across gaps, though such gaps were rare. Each light curve's mean was subtracted. Following Papadakis & Lawrence (1993) and Vaughan (2005), the periodogram was logarithmically binned by a factor of ∼0.20 in the logarithm (roughly a factor of 1.6 in f) to produce the observed PSD, $P(f)$; the two lowest temporal frequency bins were widened to accommodate three periodogram points. The constant level of power due to Poisson noise was not subtracted from these PSDs, but instead modeled in the Monte Carlo analysis. The individual long-, medium-, and short-term PSDs were combined to yield the final, broadband observed PSD, which is shown in Figure 12(a). The PSD normalization of Miyamoto et al. (1991) and van der Klis (1997) was used to permit combining PSD segments from different missions; no additional renormalization of the individual measured PSDs was done.

We first tested an unbroken power-law model of the form $P(f) = A_0(f/f_0)^{-\alpha}$, where α is the power-law slope and the normalization A_0 is the PSD amplitude at f_0, arbitrarily chosen to be 10^{-6} Hz. We stepped through α from 0.0 to 3.2 in increments of 0.01. The best-fit model, plotted in Figure 12(a) as the dotted lines, was obtained for $\alpha = 1.73 \pm 0.18$. The rejection probability $R_{\rm unbr}$ was 0.948. The residuals are plotted in Figure 12(b). The errors reported here correspond to a value 1σ above $R_{\rm unbr}$ for the best-fit value on a Gaussian probability distribution. For instance, $R_{\rm unbr}$ corresponds to 1.94σ; the error on α corresponds to 2.94σ or $R_{\rm unbr} = 0.997$. (However, see Mueller & Madejski (2009) for warnings regarding using rejection probabilities as confidence regions for PSD model parameters.)

We then tested a singly broken PSD model shape of the form $P(f) = A_1(f/f_{\rm b})^{-\alpha_{\rm lo}}$ for $f \leqslant f_{\rm b}$, or $A_1(f/f_{\rm b})^{-\alpha_{\rm hi}}$ for $f > f_{\rm b}$,

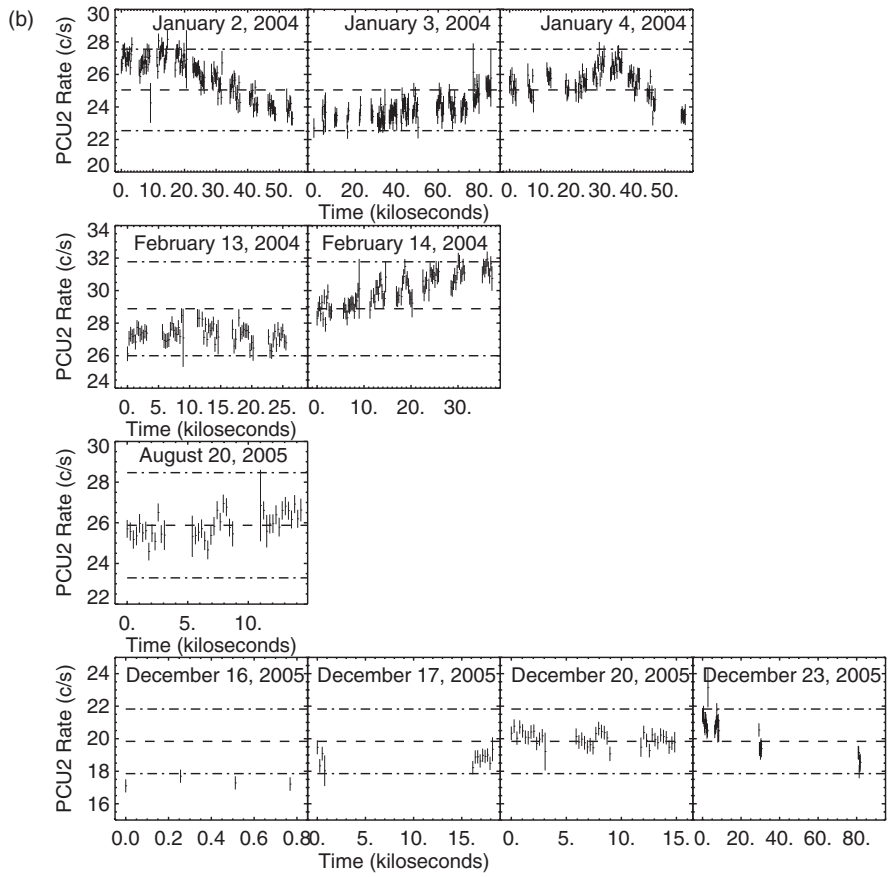

Figure 11. (Continued)

where the normalization A_1 is the PSD amplitude at the break frequency f_b, and α_{lo} and α_{hi} are the low- and high-frequency power-law slopes, respectively, with the constraint $\alpha_{lo} < \alpha_{hi}$. PSD slopes were tested in increments of 0.1, as was $\log(f_b)$. The limited amount of PSD data precluded testing more complex PSD shapes.

The best-fit model had a rejection probability R_{brkn} of 0.208 for $\log(f_b) = -(6.2^{+0.3}_{-0.2})$ (corresponding to $T_b = 18.3^{+18.3}_{-6.7}$ d), $\alpha_{hi} = 2.5^{+0.4}_{-0.1}$, and $\alpha_{lo} = 0.9^{+0.3}_{-0.2}$. These errors correspond to values 1σ above the rejection probability for the best-fit value on a Gaussian probability distribution; the best-fit model's rejection probability corresponds to 0.27σ; the errors correspond to $R_{brkn} = 0.796$ or 1.27σ (Markowitz et al. 2003). The amplitude A_1 was $7.9^{+3.1}_{-2.3} \times 10^4$ Hz^{-1}; the best-fit value of $A_1 \times f_b$ is 0.05, broadly consistent with values of ∼0.01–0.02 measured for Seyferts.

The best-fit model is shown in Figure 12(a) as a solid line, and as shown in Figure 12(c), the residuals are much smaller compared to the unbroken power-law fit, particularly in the ASM PSD segment. Following Markowitz et al. (2003), using the ratio of likelihoods of acceptance L_{brkn}/L_{unbr} ($L_{brkn} \equiv 1 - R_{brkn}$; $L_{unbr} \equiv 1 - L_{unbr}$), the PSD break was significant at $\sim 15\sigma$.

Can the flattening in PSD slope seen in the ASM PSD segment be an artifact? For an energy spectrum with the shape of that for Cen A falling off rapidly below ∼3 keV, the spectrum-weighted effective area of the ASM peaks near roughly 4 keV, while that for the PCA peaks near 5–6 keV, so the difference in average photon energy may play a minor role at best. PSD power-law slopes above the break have been observed to flatten with increasing photon energy for an assumed energy-independent f_b (e.g., Nandra & Papadakis 2001; Vaughan & Fabian 2003), but the effect is in the opposite sense to that observed in the Cen A PSD. Finally, as the ASM light curve is virtually continuous, a constant level of power due to aliasing is not expected in this PSD segment. We conclude that the break in the PSD is real. Current *RXTE* monitoring to bridge the "gap" in the current PSD and cover the temporal frequency range $10^{-6.6}$ to $10^{-5.2}$ Hz is on-going and will be useful in further constraining the break frequency and PSD power-law slopes.

Finally, the effect of the observed evolution in line-of-sight column density N_H on the ASM PSD can be estimated as follows. The increase in N_H corresponds to a reduction in the observed 2–10 keV flux by ∼35%. We added an ∼2 year long trend with flux increasing/decreasing by 35% during 2003–2004 to the binned ASM light curve as a rough estimate of the intrinsic or unabsorbed light curve. The observed 2–10 keV flux of Cen A during 2003–2004 was below the long-term average, and so this action changed the fractional variability amplitude F_{var} (Vaughan et al. 2003) only slightly: a decrease of 3% from $F_{var} = 29\%$ to 26%. That is, the unabsorbed light curve is slightly less variable than the observed light curve; the intrinsic PSD, compared to the observed PSD, may be lower by up to 17% in linear space, or 0.07 in log space, on temporal frequencies $\lesssim 1.0 \times 10^{-8}$ Hz. In other words, the intrinsic broadband PSD may bend even more strongly than the observed PSD, albeit by a very small amount.

5. DISCUSSION AND CONCLUSIONS

A summary of the results from the *RXTE* observations includes (1) the power-law index was constant (to within a few

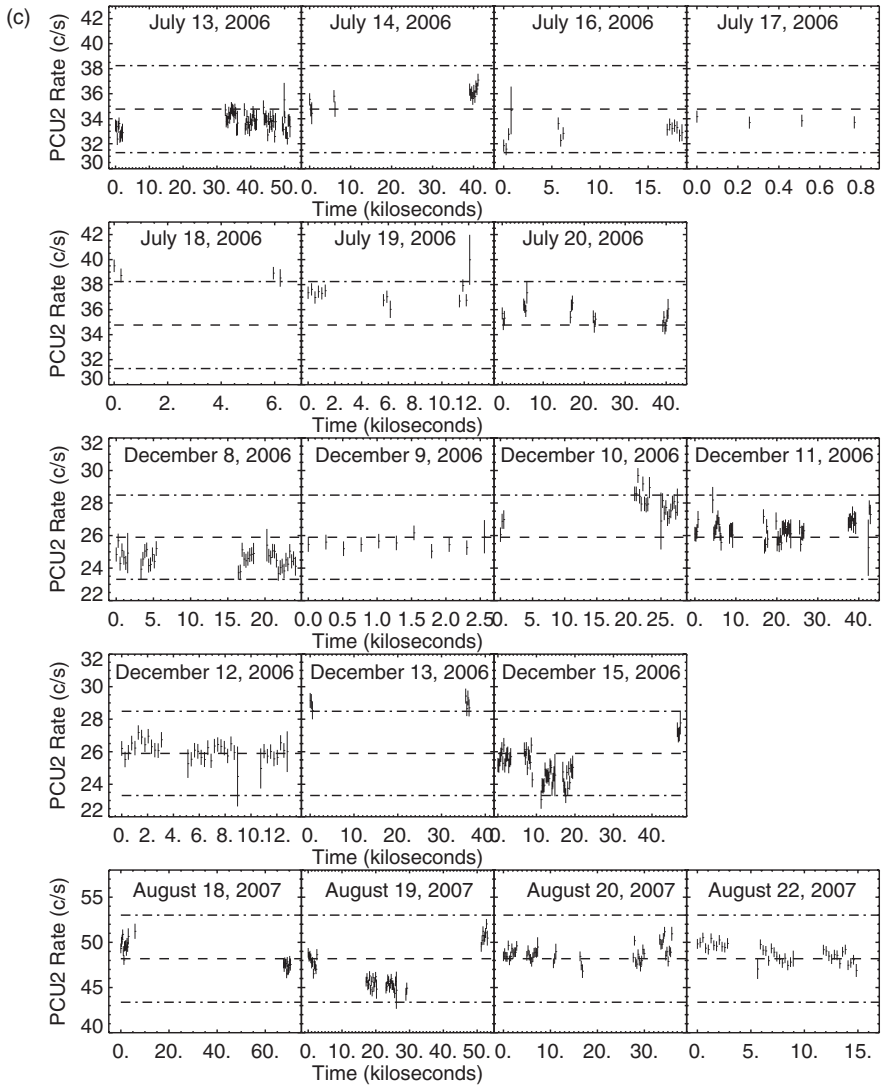

Figure 11. (Continued)

percent) and independent of 2–10 keV power-law flux, which varied by a factor of three, (2) the column density experienced a factor of two variation within a 1–4 year time span, (3) the iron line flux was independent of the power-law flux, (4) the equivalent width was not proportional to the iron line flux, but varied inversely with the power-law flux, (5) the iron line flux was not correlated with the column density variations, (6) a Compton reflection component was not detected, and (7) any high-energy spectral rollover was greater than ∼500 keV and could be as high as 2 MeV.

In order to establish a picture of the geometry of the X-ray continuum emitter and the circumnuclear accreting material, these results must be combined with results from sub-parsec scale mid-infrared observations that reveal a nuclear, molecular torus with 0.6 pc diameter and a 62°.6 inclination dusty disk (Burtscher et al. 2010), theoretical work describing the torus as a clumpy medium (Nenkova et al. 2002; Nenkova et al 2008a; Nenkova et al. 2008b), and when combined with the steeper spectra seen at GeV and TeV energies, the combined X-ray/gamma-ray data define the general shape and location of the blazar inverse Compton peak.

In the following sections, we discuss the implications of the iron line diagnostics of the circumnuclear gas, inferences about a clumpy torus, the X-ray variability, the implications of not observing a correlation between the power-law index and the power-law flux, and the possible origin of the continuum emission. Our overall conclusions are then presented.

5.1. Fe Kα Line Diagnostics of the Circumnuclear Gas

The lack of a strong observed Compton reflection component suggests that the bulk of the circumnuclear material is Compton-thin, or, if there does exist Compton-thick circumnuclear gas, it does not contribute significantly to the observed spectrum and/or is poorly illuminated by the central X-ray source. In either case, the bulk of the observed Fe Kα emission line originates in Compton-thin gas, with at most a negligible contribution from Compton-thick gas.

The Fe emission line's observed equivalent width EW_{obs} can be used as a diagnostic of the geometry of the Fe-line emitting gas under certain assumptions. For the moment, let us assume a simplified geometry in which the Fe-line emitting gas is distributed in an optically thin, uniform spherical shell with line-of-sight column density N_H and a covering fraction as seen from the central X-ray continuum source f_{cov}. We use $EW_{obs} = 90 \pm 10$ eV, the long-term average obtained by

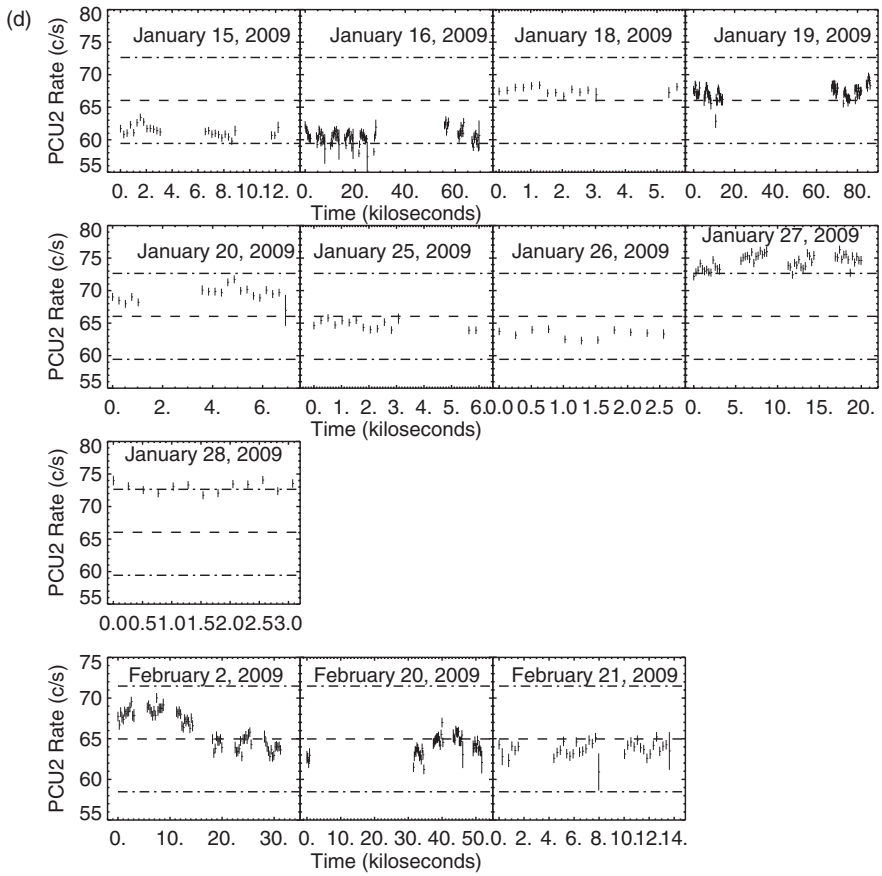

Figure 11. (Continued)

Rivers et al. (2011) from fits to the total summed PCA + HEXTE spectrum. We can then use Equation (5) from Murphy & Yaqoob (2009) to relate EW_{obs} to N_H and f_{cov}. Assuming solar abundances ($Z_{Fe} = 1$), the abundances of Wilms et al. (2000), and an illuminating continuum with $\Gamma = 1.83$, we find $EW_{obs} = 40\,eV \times (N_H/10^{23}\,cm^{-2}) \times f_{cov}$. A value of N_H of $2.1 \times 10^{23}\,cm^{-2}$ along with $f_{cov} = 1$ will yield $EW_{obs} = 90\,eV$. Similarly, if the long-term average observed line of sight N_H from Rivers et al. (2011), $1.5 \times 10^{23}\,cm^{-2}$, is used, a covering fraction of unity and $Z_{Fe} = 1.5$ will yield the same value of EW_{obs}. That is, for all values of N_H less than a few times $10^{23}\,cm^{-2}$, covering fractions near unity are required. This may indicate that the Fe-line emitting gas is highly spatially extended as seen from the central source, consistent with the observed lack of strong variability in the intensity of the Fe line between 1996 and 2009, with response to the most rapid continuum variations getting smeared out.

Alternatively, if the Fe-line emitting gas is not distributed uniformly, the observed equivalent width can still be attained with gas having a column density near $10^{24}\,cm^{-2}$ and f_{cov} near one-fifth; a torus-like structure lying mostly out of our line of sight would be consistent with this scenario. Following Figure 8 of Murphy & Yaqoob (2009), assuming a torus-like structure with N_H of a few $\times 10^{23}\,cm^{-2}$ inclined so that it is not intersecting our line of sight, $EW_{obs} \sim 90\,eV$ can be obtained if $Z_{Fe} \sim 2$. If this torus does intersect our line of sight (consistent with full-covering absorption observed in hard X-ray spectra of Cen A), an EW_{obs} near 100 eV can be attained with $Z_{Fe} \sim 1$.

We also applied the new model "MYTorus" (Murphy & Yaqoob 2009) to our time-averaged data. This model is self-consistent and includes Compton reflection, Fe line emission, and line-of-sight absorption due to a dusty circumnuclear torus. It has the benefit of being a physical model but also has the drawback of requiring certain simplifications and assumptions made about the geometry of the torus (namely, that the half-opening angle of the torus is 60°, the torus cross section is circular, and the torus is uniform in density). Note that "MYTorus" also uses the abundances of Anders & Grevesse (1989) which yield lower values of N_H than those of Wilms et al. (2000), which are used throughout the above analyses. However it gives us certain insights into possible configurations of the material surrounding Cen A.

The scenario tested by MYTorus was that of a torus that intercepts the line of sight, accounting for the observed absorption. In this case, we obtained an inclination angle for the torus of >70° to the line of sight and a column density of $N_H = 1.11 \pm 0.03 \times 10^{23}\,cm^{-2}$. The torus was able to account for only half of the Fe line flux observed and did not include any significant contribution from the Compton reflection hump. An additional toroidal component of material with column density $N_H = 1.3 \pm 0.5 \times 10^{23}\,cm^{-2}$ outside of the direct line of sight to the nucleus can account for the additional Fe line flux.

5.2. Inferences about a Clumpy Torus

Temporal variations in column density are very common in Seyfert galaxies on various timescales (Risaliti et al. 2002; Lamer et al. 2003). In Cen A, the line-of-sight X-ray column density measured in 2003 March, 2004 January, and 2004 February was (2.3, 2.6, 2.4) $\times 10^{23}\,cm^{-2}$, respectively, whereas before and after it was about $1.6 \times 10^{23}\,cm^{-2}$. For the following discussion, we assume that this represented the passage through

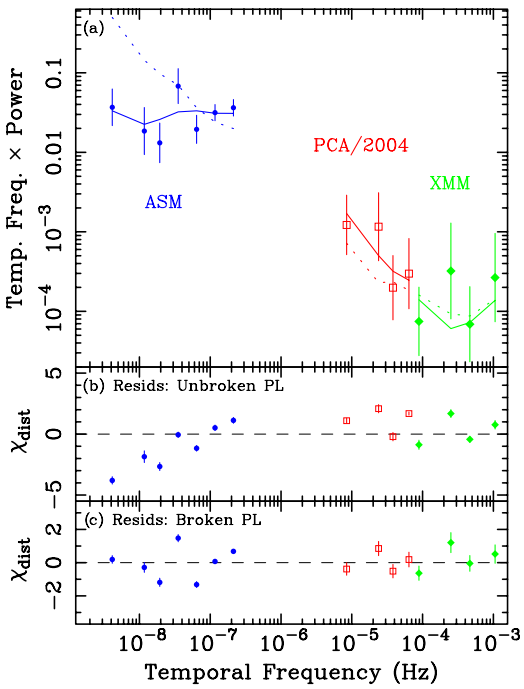

Figure 12. Power spectral density function for Cen A, derived from *RXTE* and *XMM* observations. In the top panel, the data points denote the observed binned PSD, with uncertainties on each point derived from the Monte Carlo simulation procedure (Uttley et al. 2002). The dotted and solid lines denote the best-fit unbroken and broken power-law models, respectively; both are plotted in "data" space and contain the distortion effects inherent in PSD measurement. The χ_{dist} residuals to the unbroken and singly broken power-law fits are given in panels (b) and (c), respectively. χ_{dist} compares the model PSD (from the Monte Carlo simulation procedure) and observed PSD, using the distribution estimated from the simulations (see Uttley et al. 2002, for details).

(A color version of this figure is available in the online journal.)

our line of sight of a single clump of matter in the circumnuclear torus representing a change in $N_H \sim 1 \times 10^{23}$ cm^{-2}.

The clumpy torus model of Nenkova (Nenkova et al. 2002; Nenkova et al 2008a; Nenkova et al. 2008b) parameterizes the number of clumps along the line of sight at an angle Θ to the torus equatorial pole as $N_{LOS}(90^\circ - \Theta)$. The model also characterizes the number of clumps along the line of sight as an exponentially decreasing function of Θ, i.e., the maximum number of clumps is seen in the equatorial plane of the torus, and the number decreases with angle from the plane. If one clump passing through the Cen A line of sight has a column density that is a large fraction of the total column density seen, as is the case here, one can infer that the line of sight only contains a few clumps. This, in turn, may be interpreted as viewing Cen A at an angle to the torus equatorial plane, such that our line of sight passes through the outer region of the torus.

Furthermore, using the angle of the torus to the line of sight as 62.°6 (Burtscher et al. 2010) and $N_{LOS}(90^\circ - \Theta) = N_0 \exp(-(\Theta/\sigma)^2)$, where N_0 is the average number of clouds along the equatorial direction and σ characterizes angular distribution of clouds (Ramos Almeida et al. 2009), we find for $\Theta = 62.°6$, $\sigma = 60^\circ$ (Ramos Almeida et al. 2009), and $N_{LOS}(90^\circ - \Theta) = 3$, that $N_0 = 8$. This is in accordance with the statement in Nenkova et al. (2008b) that "N_0 is likely no larger than ~10–15 at most," since a larger number would produce an infrared bump that is not seen. Therefore, viewing Cen A through the outer edges of the torus is consistent with the clumpy torus model.

If N_H for a representative clump is 1×10^{23} cm^{-2}, then eight of them along the torus equatorial plane imply that the material in the equatorial plane may be close to being Compton-thick (~10^{24} cm^{-2}), but this value will drop as one goes farther from the plane of the torus, and the majority of the torus will be Compton-thin. Thus, the Compton thick aspects of the circumnuclear torus may be restricted to near the equatorial plane, and would explain the lack of a detected Compton reflection component. In addition, we have speculated previously that the high-energy radiation from the nucleus could be anisotropic with very little if any of it illuminating the Compton-thick material (Rothschild et al. 2006). A combination of a minimum of Compton-thick material and an anisotropic radiation pattern may provide a more complete explanation for the lack of a Compton hump in Cen A.

From Figure 4 (middle), we can estimate how long the clump took to pass through our line of sight. Assuming a sharp transition in N_H as the clump passed into and out of the line of sight, we estimate a duration T of a minimum of ~1 year and a maximum of ~4 years. Assuming a torus diameter of 0.6 pc (Meisenheimer et al. 2007) and a black hole mass M_{BH} of $6 \times 10^7\ M_\odot$ (Cappellari et al. 2009; Neumayer et al. 2010), the Keplerian velocity V_K of the clump can be used to estimate its linear size, if one knew the radial position of the clump within the torus. Using radial values of the IR torus of $R_K \sim 0.1$ to ~0.3 pc, we find the velocity of the cloud $V_K = (GM_{BH}/R_K)^{0.5}$ to be on the order of 10^3 km s^{-1} and has a linear dimension $L_c = V_K \times T$ on the order of 3–12 $\times$ 10^{13} m, 0.001–0.004 pc, or about one to four light days. Given the measured column density of the clump and the derived linear dimension, an inferred number density $n_c = N_H/L_c$ is on the order of 1–3 $\times$ 10^7 cm^{-3}. This yields an approximate cloud mass $M_{Cloud} = \frac{4}{3}\pi(\frac{1}{2}L_c)^3 m_p n_c \approx 1 \times 10^{30}$ g, or about one Jupiter mass, where m_p is the proton mass. The linear dimension of the cloud is about a thousand times larger than those determined by Risaliti (2010) for clouds in the broad line region, while the density is three to four orders of magnitude smaller. The duration of the transiting event here is much longer than those seen in, e.g., NGC 1365 (Risaliti et al. 2009a, 2009b) and NGC 3227 (Lamer et al. 2003), which lasted for days to a few months, and were consistent with absorbing clouds in the optical broad line region of these objects. The lower density inferred from the Cen A absorption event could be due to the clouds in Cen A being significantly further away from the supermassive black hole than those inferred for NGC 1365 or NGC 3227.

5.3. X-ray Variability of Cen A

We can compare the break inferred in the observed PSD of Cen A with those breaks measured in the PSDs of other Seyfert AGNs by using the empirical relation between T_b, M_{BH}, and $\dot{m}$ quantified by McHardy et al. (2006). This exercise relies on the assumption that accretion onto the supermassive black hole in Cen A proceeds via the same mechanism and with the same efficiency of radiation as the Seyferts used in the sample of McHardy et al. (2006). We assume a black hole mass of $6 \times 10^7\ M_\odot$, the average of the estimates discussed in Section 1. The long-term, unabsorbed, 2–10 keV luminosity, L_{2-10} (Rivers et al. 2011), is 8.6×10^{41} erg s^{-1}. The bolometric luminosity, L_{bol}, is estimated to be 8×10^{42} erg s^{-1} (yielding an inferred accretion rate relative to Eddington of 0.1%), assuming a conversion factor $L_{bol}/L_{2-10} = 9$ (Marconi et al. 2004). The best-fit empirical relation of McHardy et al. (2006), $\log(T_b(\text{days})) = 2.10 \log(M_{BH}/10^6\ M_\odot) - 0.98 \log(L_{bol}/10^{44}\ \text{erg s}^{-1}) - 2.32$, yields a predicted break timescale $T_{b,pred}$ of 317 days, which corresponds to a break frequency of 3.7×10^{-8} Hz. The value

of $T_{\rm b,pred}$ is a factor of $\sim 17^{+36}_{-13}$ higher than the observed PSD break timescale ($T_{\rm b} = 18.3^{+18.3}_{-6.7}$) measured above for Cen A.

The sample used by McHardy et al. (2006) was derived from mainly radio-quiet Seyferts accreting at $\dot{m}$ of a few percent or more, and it is thus conceivable that radio-loud sources and/or sources accreting at very low values of $\dot{m}$ do not strictly adhere to the relation derived by McHardy et al. (2006). However, the measured PSDs for the radio-loud AGN 3C 120 and the low-luminosity AGN NGC 4258 seem to be at least roughly consistent with the relation. 3C 120 has $M_{\rm BH} \sim 5 \times 10^7\, M_\odot$ and $\dot{m} \sim 0.31$ (Vasudevan & Fabian 2009), which yields $T_{\rm b,pred} = 1.1$ days. Marshall et al. (2009) and Chatterjee et al. (2009) have each measured the X-ray PSD and found best-fit values of $T_{\rm b} = 6.5$ days and 1.2 days, respectively, consistent with $T_{\rm b,pred}$, considering the errors on $M_{\rm BH}$, $\dot{m}$, and $T_{\rm b}$. NGC 4258's black hole mass is well determined via mega masers, at $3.9 \times 10^7\, M_\odot$ (Herrnstein et al. 1999), and $\dot{m} = 10^{-4}$ (Lasota et al. 1996), so that $T_{\rm b,pred}$ is about 2000 days, consistent with the lower limit of $T_{\rm b} = 4.5$ days measured by Markowitz & Uttley (2005). We speculate that different physical mechanisms may dominate the observed X-ray variability in Seyferts and in radio-loud and/or low-$\dot{m}$ AGNs such as Cen A. That is, in such objects, the X-ray emission may be dominated by emission from a jet component versus that coming from a corona associated with the accretion disk (as in 3C 120 and the radio-quiet Seyferts).

5.4. Lack of a Power-law Flux–Power-law Index Correlation

As presented in Figure 7, no correlation was seen in the plot of power-law index versus unabsorbed 2–10 keV power-law flux, when the flux varied over a factor of three (3–10×10^{-10} erg cm^{-2} s^{-1}). This is in contrast to what is commonly reported for Seyfert 1s in the 2–10 keV band (e.g., Shih et al. 2002; Papadakis et al. 2002), where the phenomenon of increasing flux being positively correlated with increasing power-law indices is virtually ubiquitous. All of the objects for which this correlation was seen are radio-quiet Seyferts. While the radio-quiet Seyferts have a positive correlation, a relativistically broadened Fe Kα emission component in about 2/3 of the cases (Nandra et al. 2007), and significant Compton reflection components, Cen A exhibits none of these, and has a powerful jet. Perhaps the anisotropic radiation pattern at the base of the Cen A jet only illuminates the accretion disk minimally, if at all, but does illuminate a portion of the clumpy torus. This could explain the lack of a measured Compton reflection component from the disk, if the disk is indeed Compton-thick. If the power-law/flux correlation originates from processes associated with soft photon production and subsequent up-scattering of them by the hot electrons in the accretion disk corona (e.g., Haardt & Maraschi 1993), the anisotropic flux distribution mentioned above would minimize this process in Cen A. This lack of a power-law index/power-law flux correlation may also be explained by a lack of soft photons due to the presence of a radiatively inefficient accretion flow, (e.g., Narayan et al. 1998; Quataert 2001), and thus a lack of disk-produced soft photons, which are the basis for Comptonization models of hard X-ray emission in Seyferts.

5.5. Continuum Emission from the Jet in Cen A

Chiaberge et al. (2001) constructed the first spectral energy distribution (SED) for Cen A showing that the SED consisted of two components: a synchrotron component in the sub-millimeter to near-infrared and a second higher energy SSC component in the X-ray to gamma-ray range, where the latter was defined by the *CGRO* results (Kinzer et al. 1995; Steinle et al. 1998). Later, Lubiński (2009) presented the *INTEGRAL*/IBIS spectrum of Cen A extending to 400 keV or greater as a single power law. The lack of a significant deviation from a power law up to energies as high as 2 MeV, as inferred from *RXTE*, can be interpreted in the misoriented BL Lac scenario (Chiaberge et al. 2001) as having the X-ray emission from the low-energy side of the SSC hump, viewed at a large angle from the jet direction. Despite the overall SED being reminiscent of blazars, Cen A's X-ray spectrum exhibits two signatures of Seyferts and quasars: a high column density of absorbing gas in the line of sight and an iron emission line. In the Cen A case, the bright hard X-ray continuum emission may originate at the base of the jet, yet from behind the absorbing line-of-sight material in contrast to what is commonly observed from blazars. A jet origin to the continuum has also been put forth for FR I radio galaxy cores by Evans et al. (2006), but these authors associate low absorption ($<5 \times 10^{22}$ cm^{-2}) with sources having the hard X-ray emission associated with a jet. In this regard, Cen A may be a counter example.

The nature of the accretion flow near the black hole may contribute to defining the difference in nature between low-luminosity, radio-loud AGNs, such as Cen A, and radio-quiet Seyfert AGNs, since a radiatively inefficient flow may be responsible for launching jet outflows (e.g., Körding et al. 2006). In this case, one would not have the soft photons for subsequent upscattering by the hot electrons in the accretion disk corona (Haardt & Maraschi 1993). In Cen A, the accretion disk may only supply matter to the base of the jet and into the black hole, but may not make any contribution in terms of observational X-ray signatures.

5.6. Conclusions

Over more than a decade of observing, Cen A has shown remarkably stable spectral behavior. Both the power-law index and the flux of the iron line have remained essentially constant, in contrast to the range in power-law flux and column density, which have varied by a factor of three and two, respectively. The stability of the power-law index over the past 40 years (with the exception of the early 1970s when it flattened considerably Baity et al. 1981) implies a stability of the processes generating the continuum at the base of the jet. The spectral aspects of these processes, i.e., the shape of the electron distribution and electron optical depth, must therefore be relatively insensitive to the variations in the accretion rate experienced at the base of the jet, which is assumed to be directly related to the overall flux observed. From this we infer that the mass accretion rate in the inner portions of the accretion disk ($\dot{m} \approx L_X/L_{\rm Edd} \sim 10^{-4}$) has remained within the range where the radiation efficiency is relatively unchanged even though the luminosity (a tracer of the mass accretion rate) has varied by a factor of three.

Our observations with *RXTE* have led to the conclusions that we are viewing the supermassive black hole at the nucleus of this active radio galaxy through the outer portions of a clumpy molecular torus which is mainly Compton-thin, but may approach being Compton-thick only at or near its equator. The Compton-thin torus may then occupy a large solid angle as viewed from the Cen A nucleus in order to be the site of the iron line emitting material.

The variability characteristics, when compared to Seyferts, imply that the accretion disk is not the location of the >3 keV

X-ray flux, but that SSC scattering in the base of the jet may be responsible. In the case of Cen A, the bright hard X-ray continuum emission may originate at the base of the jet, yet from behind the absorbing line-of-sight material in contrast to what is commonly observed from blazars.

The authors acknowledge the excellent comments from the anonymous referee. We gratefully acknowledge NASA contract NAG5-30720 and NASA grants NNX08AY11G and NNX09AG79G for support of this analysis.

REFERENCES

Abdo, A. A., et al. 2010a, Science, 328, 725
Abdo, A. A., et al. 2010b, ApJ, 719, 1433
Aharonian, A. G., et al. 2009, ApJ, 695, L40
Anders, E., & Grevesse, N. 1989, Geochim. Cosmochim. Acta, 53, 197
Arnaud, K. A. 1996, in ASP Conf. Ser. 101, Astronomical Data Analysis Software and Systems, ed. G. Jacoby & J. Barnes (San Francisco, CA: ASP), 17
Baade, W., & Minkowski, R. 1954, ApJ, 119, 215
Baity, W. A., et al. 1981, ApJ, 244, 429
Bolton, J. G., Stanley, G. J., & Slee, O. B. 1949, Nature, 164, 101
Bowyer, C. S., Lampton, M., Mack, J., & de Mendonca, F. 1970, ApJ, 161, L1
Burbidge, G. R., & Burbidge, E. M. 1957, ApJ, 125, 1
Burtscher, L., Meisenheimer, K., Jaffe, W., Tristram, K. R. W., & Röttgering, H. J. A. 2010, PASA, 27, 490
Cappellari, M., Neumayer, N., Reunanen, J., van der Werf, P. P., de Zeeuw, P. T., & Rix, H.-W. 2009, MNRAS, 394, 660
Chatterjee, R., et al. 2009, ApJ, 704, 1689
Chiaberge, M., Capetti, A., & Celotti, A. 2001, MNRAS, 324, L33
Cooke, B. A., Pounds, K. A., Stewardson, E. A., & Adams, D. J. 1967, ApJ, 150, L189
Edelson, R., & Nandra, K. P. 1999, ApJ, 514, 682
Evans, D. A., Kraft, R. P., Worrall, D. M., Hardcastle, M. J., Jones, C., Forman, W. R., & Murray, S. S. 2004, ApJ, 612, 786
Evans, D. A., Worrall, D. M., Hardcastle, M. J., Kraft, R. P., & Birkinshaw, M. 2006, ApJ, 642, 96
Fanaroff, B. L., & Riley, J. M. 1974, MNRAS, 167, 31P
Ferrarese, L., Mould, J. R., Stetson, P. B., Tonry, J. L., Blakeslee, J. P., & Ajhar, E. A. 2007, ApJ, 654, 186
Green, A., McHardy, I., & Lehto, H. 1993, MNRAS, 265, 664
Haardt, F., & Maraschi, L. 1993, ApJ, 413, 507
Harries, J., McCracken, K. G., Francey, R. J., & Fenton, A. J. 1967, Nature, 215, 38
Harris, G. L. H., Rejkuba, M., & Harris, W. H. 2010, PASA, 27, 457
Herrnstein, J. R., et al. 1999, Nature, 400, 539
Horiuchi, S., Meier, D. L., Preston, R. A., & Tingay, S. J. 2006, PASJ, 58, 211
Hui, X., Ford, H. C., Ciardullo, R., & Jacoby, G. H. 1993, ApJ, 414, 463
Humason, M. L., Mayall, N. U., & Sandage, A. R. 1956, AJ, 61, 97
Israel, F. P. 1998, ARA&A, 8, 237
Jahoda, K., Markwardt, C. B., Radeva, Y., Rots, A. H., Stark, M. J., Swank, J. H., Strohmayer, T. E., & Zhang, W. 2006, ApJS, 163, 401
Kataoka, J., Tanahata, C., Kawai, N., Takahara, F., Takahashi, T., Edwards, P. G., & Makino, F. 2002, MNRAS, 336, 932
Kataoka, J., et al. 2001, ApJ, 560, 659
Kinzer, R. L., et al. 1995, ApJ, 449, 105
Körding, E. G., Fender, R. P., & Migliari, S. 2006, MNRAS, 369, 1451
Kraft, R. P., Kregenow, J. M., Foreman, W. R., Jones, C., & Murray, S. S. 2001, ApJ, 560, 675
Kraft, R. P., Vázquez, S. E., Foreman, W. R., Jones, C., Murray, S. S., Hardcastle, M. J., Worrall, D. M., & Churazov, E. 2003, ApJ, 592, 129
Kraft, R. P., et al. 2000, ApJ, 531, L9
Krajnović, D., Sharp, R., & Thatte, N. 2007, MNRAS, 374, 385
Lamer, G., Uttley, P., & McHardy, I. M. 2003, MNRAS, 342, L41
Lasota, J.-P., Abramowicz, M. A., Chen, X., Krolik, J., Narayan, R., & Yi, I. 1996, ApJ, 462, 142
Lawrence, A., & Papadakis, I. E. 1993, ApJ, 414, L85
Lawrence, A., Watson, M., Pounds, K., & Elvis, M. 1987, Nature, 325, 694
Lewin, W. H. G., Clark, G. W., & Smith, W. B. 1968, ApJ, 152, L49
Lubiński, P. 2009, A&A, 496, 557
Magdziarz, P., & Zdziarski, A. A. 1995, MNRAS, 273, 837
Marconi, A., Pastorini, G., Axon, D. J., Capetti, A., Macchetto, D., Koekemoer, A. M., & Schreier, E. J. 2006, A&A, 448, 921
Marconi, A., Risaliti, G., Gilli, R., Hunt, L. K., Maiolino, R., & Salvati, M. 2004, MNRAS, 351, 169
Markowitz, A., & Uttley, P. 2005, ApJ, 625, L39
Markowitz, A., et al. 2003, ApJ, 593, 96
Markowitz, A. G., et al. 2007, ApJ, 665, 209
Marscher, A. P., Jorstad, S. G., Aller, M. F., McHardy, I., Balonek, T. J., Teräsranta, H., & Tosti, G. 2004, in AIP Conf. Proc., Vol. 714, X-RAY TIMING 2003: Rossi and Beyond, ed. P. Kaaret, F. K. Lamb, & J. H. Swank (Melville, NY: AIP), 167
Marshall, K., Ryle, W. T., Miller, H. R., Marscher, A. P., Jorstad, S. G., Chicka, B., & McHardy, I. M. 2009, ApJ, 696, 601
McHardy, I. M., Koerding, E., Knigge, C., Uttley, P., & Fender, R. P. 2006, Nature, 444, 730
Meisenheimer, K., et al. 2007, A&A, 471, 453
Mills, B. Y. 1952, Nature, 170, 1063
Mills, B. Y. 1953, Aust. J. Phys., 6, 452
Miyamoto, S., Kimura, K., Kitamoto, S., Dotani, T., & Ebisawa, K. 1991, ApJ, 383, 784
Mueller, M., & Madejski, G. 2009, ApJ, 700, 243
Müller, C., Kadler, M., Ojha, R., Froom, C., Ros, E., Rothschild, R. E., & Wilms, J. 2010, in Fermi Meets Jansky—AGN in Radio and Gamma-Rays, ed. T. Savolainen et al. (Bonn: Max Planck Institute for Radio Astronomy; arXiv:1006.1486)
Murphy, K. D., & Yaqoob, T. 2009, MNRAS, 397, 1549
Nandra, K., O'Neill, P. M., George, I. M., & Reeves, J. N. 2007, MNRAS, 382, 194
Nandra, K., & Papadakis, I. E. 2001, ApJ, 554, 710
Narayan, R., Mahadevan, R., & Quateart, E. 1998, in Theory of Black Hole Accretion Disks, ed. M. A. Abramowicz, G. Bjornsson, & J. E. Pringle (Cambridge: Cambridge Univ. Press), 148
Nenkova, M., Ivesić, Ž, & Elitzur, M. 2002, ApJ, 570, L9
Nenkova, M., Sirocky, M. M., Ivesić, Ž, & Elitzur, M. 2008a, ApJ, 685, 147
Nenkova, M., Sirocky, M., Nikutta, R., Ivezić, Ž., & Elitzur, M. 2008b, ApJ, 685, 160
Neumayer, N., Cappellari, M., van der Wert, P., Reunanen, J., Rix, H.-W., de Zeeuw, T., & Davies, R. 2010, The Messenger, 139, 36
Ojha, R., et al. 2010, A&A, 519, A45
Oppenheim, A., & Shafer, R. 1975, Digital Signal Processing (Englewood Cliffs, NJ: Prentice-Hall)
Papadakis, I. E., & Lawrence, A. 1993, MNRAS, 261, 612
Papadakis, I. E., Petrucci, P. O., Maraschi, L., McHardy, I. M., Uttley, P., & Haardt, F. 2002, ApJ, 573, 92
Quataert, E. 2001, in ASP Conf. Proc., Vol. 224, Probing the Physics of Active Galactic Nuclei, ed. B. M. Peterson, R. W. Pogge, & R. S. Polidan (San Francisco, CA: ASP), 71
Ramos Almeida, C., et al. 2009, ApJ, 702, 1127
Rejkuba, M. 2004, A&A, 413, 903
Risaliti, G. 2010, in IAU Symp. 267, Co-Evolution of Central Black Holes and Galaxies, ed. B. M. Peterson, R. S. Somerville, & T. Storchi-Bergmann (Cambridge: Cambridge Univ. Press), 299
Risaliti, G., Elvis, M., & Nicastro, F. 2002, ApJ, 571, 234
Risaliti, G., et al. 2009a, MNRAS, 393, L1
Risaliti, G., et al. 2009b, ApJ, 696, 160
Rivers, E., Markowitz, A., & Rothschild, R. E. 2011, ApJS, 193, 3
Rothschild, R. E., et al. 1998, ApJ, 496, 538
Rothschild, R. E., et al. 2006, ApJ, 241, 801
Shih, D. C., Iwasawa, K., & Fabian, A. C. 2002, MNRAS, 333, 687
Silge, J. D., Gebhardt, K., Bergmann, M., & Richstone, D. 2005, AJ, 130, 406
Stark, J. P., Davison, P. J. N., & Culhane, J. L. 1976, MNRAS, 174, 35
Steinle, H., et al. 1998, A&A, 330, 97
Uttley, P., McHardy, I. M., & Papadakis, I. E. 2002, MNRAS, 332, 231
van der Klis, M. 1997, in Statistical Challenges in Modern Astronomy II, ed. G. J. Babu & E. D. Feigelson (New York: Springer), 321
Vasudevan, R. V., & Fabian, A. C. 2009, MNRAS, 392, 1124
Vaughan, S. 2005, A&A, 431, 391
Vaughan, S., Edelson, R., Warwick, R. S., & Uttley, P. 2003, MNRAS, 345, 1271
Vaughan, S., & Fabian, A. C. 2003, MNRAS, 341, 496
Verner, D. A., Ferland, G. J., Korista, K. T., & Yakovlev, D. G. 1996, ApJS, 465, 487
Wade, C. M. 1959, Aust. J. Phys., 12, 47
Wilms, J., Allen, A., & McCray, R. 2000, ApJ, 542, 914